

Special Collection:

Fold-and-Thrust Belts: Evolution and Dynamics at All Spatiotemporal Scales

Key Points:

- The Tempa Roccarossa mélange shows a peak T of $250 \pm 10^\circ\text{C}$ partially due to shear heating
- Maximum burial of the Tempa Roccarossa mélange accounts to a depth of at least 12 km
- Unloading processes account for the thermal breaks between the different thrust sheets

Supporting Information:

Supporting Information may be found in the online version of this article.

Correspondence to:

S. Vitale,
stefano.vitale@umina.it

Citation:

Vitale, S., Cardello, G. L., Cavalcante, F., Fedele, L., Lanari, P., Mehmood, M., et al. (2025). The anchimetamorphic tectonic mélange of Tempa Roccarossa (southern Apennines, Italy): Insights on the kinematic and thermobaric evolution of the upper miocene-pleiocene orogenic wedge. *Tectonics*, 44, e2024TC008503. <https://doi.org/10.1029/2024TC008503>

Received 8 JUL 2024

Accepted 23 APR 2025

Author Contributions:

Conceptualization: S. Vitale, G. L. Cardello, F. Cavalcante, S. Ciarcia
Data curation: S. Vitale, F. Cavalcante, L. Fedele, M. Mehmood
Formal analysis: S. Vitale, F. Cavalcante, L. Fedele, P. Lanari, M. Mehmood, L. Peruzzo
Funding acquisition: S. Vitale
Investigation: S. Vitale, F. Cavalcante, L. Fedele, M. Mehmood, S. Ciarcia
Methodology: S. Vitale, G. L. Cardello, F. Cavalcante, L. Fedele, P. Lanari

© 2025. The Author(s).

This is an open access article under the terms of the [Creative Commons Attribution License](https://creativecommons.org/licenses/by/4.0/), which permits use, distribution and reproduction in any medium, provided the original work is properly cited.

The Anchimetamorphic Tectonic Mélange of Tempa Roccarossa (Southern Apennines, Italy): Insights on the Kinematic and Thermobaric Evolution of the Upper Miocene-Pliocene Orogenic Wedge

S. Vitale¹ , G. L. Cardello², F. Cavalcante³, L. Fedele¹ , P. Lanari^{4,5}, M. Mehmood¹, J. Natale⁶ , L. Peruzzo⁷ , and S. Ciarcia⁸ 

¹Dipartimento di Scienze della Terra, dell'Ambiente e delle Risorse (DiSTAR), Università degli Studi di Napoli Federico II, Napoli, Italy, ²Dipartimento di Chimica, Fisica, Matematica e Scienze Naturali, Università di Sassari, Sassari, Italy, ³Istituto di Metodologie per l'Analisi Ambientale—CNR, Potenza, Italy, ⁴Institute of Geological Sciences, University of Bern, Bern, Switzerland, ⁵Institute of Earth Sciences, University of Lausanne, Lausanne, Switzerland, ⁶Dipartimento di Scienze della Terra e Geoambientali, Università degli Studi di Bari Aldo Moro, Bari, Italy, ⁷Istituto di Geoscienze e Georisorse—CNR, Padova, Italy, ⁸Dipartimento di Scienze e Tecnologie, Università del Sannio, Benevento, Italy

Abstract Studies of tectonic mélanges provide constraints on the evolution of active plate margins.

However, resolving the pressure-temperature trajectories of these deformed rocks, which are exhumed from low-temperature conditions, can be challenging. We analyzed a Late Miocene-Early Pliocene tectonic mélange formed in a shear zone in the southern Apennines (Basilicata, Italy), located in the hanging wall of a regional thrust, to provide estimates of temperature, pressure and strain. The mélange comprises slates with a fine-grained phyllosilicate matrix embedding larger porphyroclasts with relict S_0 bedding. Electronic microscope analysis revealed a disjunctive cleavage (S_1), partially to fully transposed by a top-to-the-E/SE crenulation cleavage (S_2) marked by white mica and chlorite. A late weak cleavage (S_3) is not accompanied by newly formed minerals. Kinematic vorticity analysis indicates a range of 20%–35% coaxial strain, whereas 3D strain analysis of deformed clasts suggests oblate strain. X-Ray Powder Diffraction analysis of grains $<2 \mu\text{m}$ indicates anchimetamorphic conditions between 200 and 250°C , with temperatures increasing by 50°C toward the thrust contact. Multi-equilibrium modeling of coarser S_1 - S_2 grains ranges from 300 to 380°C , independent of their position in the shear zone. We attribute the low-temperature range of finer grains to Apennine anchimetamorphism, whereas grains $>2 \mu\text{m}$ are likely detrital and record higher pressure-temperature conditions. Assuming a regional paleogeothermal gradient of $20^\circ\text{C}/\text{km}$, we estimate a maximum burial depth of about 12 km and a pressure of 0.32 GPa. This approach can be applied to similar contexts worldwide, providing a tool for regional tectonic reconstruction and process-oriented studies.

1. Introduction

In orogenic belts, mélanges are defined as exhumed chaotic rocks characterized by a block-in-matrix texture. They are the result of sedimentary (submarine mass transport), tectonic (thrust-related shearing), and mud-diapiric (fluid/gas-driven remobilization of mud/shales) processes (Ogata et al., 2019). They are therefore classified as sedimentary, tectonic, or diapiric (Festa et al., 2019). Hsü (1968) defines a tectonic mélange as mappable bodies of deformed rocks incorporating mixed fragments or blocks within a pervasively sheared fine-grained matrix. In general, the texture of these rocks appears chaotic due to the disruption of the original sedimentary features, resulting in a lack of internal continuity of strata (Cloos, 1983; Evans & Brown, 1986). Mélanges associated with faults or shear zones are also known as “sheared mélanges” (sensu Needham, 1995) or “asymmetric mélanges” (sensu Fisher & Byrne, 1987; Hammond, 1987).

Overall, tectonic mélanges are common in subduction zones (Cloos & Shreve, 1988; Federico et al., 2007; Kimura et al., 2012; Penniston-Dorland & Harvey, 2023; Wang et al., 2013; Zagorevski et al., 2012) and forearc basins (e.g., Chang et al., 2009; Huang et al., 2006). They can form in association with major fault zones (e.g., Brueckner et al., 2009) in accretionary complexes (e.g., Barnes & Korsch, 1991; Cloos, 1984; Kimura et al., 2012; Mazzoli, Barkham, et al., 2001; Mazzoli, Zampetti, & Zuppetta, 2001; Richter et al., 2025). During their formation, the chaotic structure of mélanges can incorporate both ‘exotic’ (extraformational or allochthonous) and ‘native’ (intraformational or autochthonous) materials (Ogata et al., 2019). The formation of the tectonic mélanges

Project administration: S. Vitale
Resources: S. Vitale
Software: P. Lanari
Supervision: S. Vitale
Validation: S. Vitale, G. L. Cardello, F. Cavalcante, L. Fedele, P. Lanari, J. Natale, S. Ciarcia
Visualization: F. Cavalcante
Writing – original draft: S. Vitale, G. L. Cardello, F. Cavalcante, L. Fedele, P. Lanari, J. Natale, S. Ciarcia

may persist for long periods, progressively incorporating younger native syn-orogenic material, including fossil content, over different deformation events (e.g., Cardello et al., 2021). Brittle-ductile transitional mélange contexts develop at their seismogenic roof décollement, where mélanges form as plate boundary fault rocks in the subduction zone (Kitamura et al., 2005).

Mélanges exhumed from more advanced metamorphic contexts are common in Alpine settings, where the lithofacies display general and pervasive retrograde greenschist facies metamorphism, along with a mylonitic transposition fabric (e.g., Roda et al., 2020; Vissers et al., 2001). At low pressure-temperature (P-T) conditions, their textures can still carry information on the originating processes (Codegone et al., 2012; Festa et al., 2010, 2012; Ogawa et al., 2011). In these contexts, microstructural and compositional studies of mélange tectonites precede in situ geochronological studies as they are crucial for investigating orogenic dynamics (e.g., Byrne, 1984; Cardello et al., 2019; Cowan, 1985; Fukui & Kano, 2007; Kimura et al., 2012; Penniston-Dorland & Harvey, 2023; Wang et al., 2013). This can be achieved by integrating thermochronological data with geochronological, biostratigraphic and petrologic constraints.

To gain insights into the processes active in tectonic mélanges, we have developed an interdisciplinary study in a key area that, besides the general processes, also allows a better definition of the geometry and evolution of the nappe stack of the southern Apennines (Italy) (e.g., Mazzoli, Barkham, et al., 2001; Mazzoli, Zampetti, & Zuppetta, 2001; Patacca & Scandone, 2007; Roure et al., 1991). This orogen is largely made of non-metamorphic terrains (e.g., Ciarcia & Vitale, 2025 and references therein). However, the studied outcrop is located on the hanging wall of a large, deep segment of a décollement that guided thrusting within the Upper Miocene-Lower Pliocene accretionary wedge, whose P-T conditions, strain, and tectonic evolution are currently poorly constrained (e.g., Catalano et al., 2004; Mazzoli, 1992). We have investigated the kinematics and the finite strain recorded by these highly deformed rocks, which were also characterized by their mineral and whole-rock geochemical compositions, to estimate the temperature and pressure associated with maximum burial. This study aims to shed light on the mechanisms and processes at work in tectonic mélanges, which accommodate most of the crustal shortening during orogenic processes, using the southern Apennines as a case study.

2. Geological Setting

The southern Apennines (Figure 1a), together with the Calabria-Peloritani Terrane (CPT), are part of the circum-Mediterranean Alpine chain (Figure 1b), formed following the subduction of the Ligurian oceanic lithosphere beneath the European plate (e.g., Doglioni, 1991; Lustrino et al., 2009; Schenk, 1980; Vitale, Ciarcia, et al., 2019). At a regional scale, the orogenic chain is characterized by the superposition of three complexes (Figure 1c; Ciarcia & Vitale, 2025 and references therein): on the top, remnants of the overriding plate, consisting of a Paleozoic Variscan crystalline basement and a sedimentary Meso-Cenozoic cover (Complex 1; Sila, Stilo, Bagni and Castagna units; Figure 1a; Amodio-Morelli et al., 1976; Ciarcia & Vitale, 2025; Schenk, 1980), superposed onto greenschist to high pressure-low temperature (HP-LT) metamorphic thrust sheets, including meta-ophiolites and slices of Adria continental cover forming the exhumated subduction channel (Complex 2; Diamante-Terranova, Malvito, Gimigliano, Frido, Lungro-Verbicaro and Cetraro units; Figure 1a; Amodio-Morelli et al., 1976; Vitale, Ciarcia, et al., 2019; Vitale, Fedele, et al., 2013). The latter, in turn, covers a fold and thrust belt (Complex 3) made of the imbrication of several thrust sheets consisting of oceanic cover on the top (Ligurian Accretionary Complex, LAC; e.g., Vitale, Ciarcia, et al., 2013; Vitale, Ciarcia, et al., 2019 and references therein), and shallow water to pelagic successions at the bottom, including Apennine Platform (ApeP), Lagonegro-Molise Basin (LMB), and buried Apulian Platform (ApuP) units; Figure 1a; Ciarcia & Vitale, 2025 and references therein). Exposed carbonates of the Puglia region and part of the Adriatic Sea represent the current foreland. The oceanic subduction started in Paleocene-Eocene times (Schenk, 1980; Vitale, Ciarcia, et al., 2019 and references therein), with the underplating of oceanic and continental slices of both overriding and downgoing plates, subsequently exhumed from the Oligocene to the Late Miocene (e.g., Ciarcia & Vitale, 2025 and references therein). Starting in the Early Miocene, an oceanic accretionary wedge formed from offscraped successions, which thrust over the western margin of the ApeP domain. Subsequently, the thrust front moved to SE/E/NE, including the LMB successions and the remnant of the ApeP successions within the orogenic wedge. Finally, at the end of the Miocene, after the complete closure of the LMB, the orogenic wedge thrust over the ApuP domain. The involvement of the thick continental lithosphere resulted in a buttressing effect and thick-skinned thrusting from the Early Pliocene to the Middle Pleistocene, with the formation of deep-seated thrust faults that also crosscut the allochthonous wedge, forming several out-of-sequence thrusts (Vitale, Prinzi, et al., 2020). In the Early Pleistocene, post-orogenic

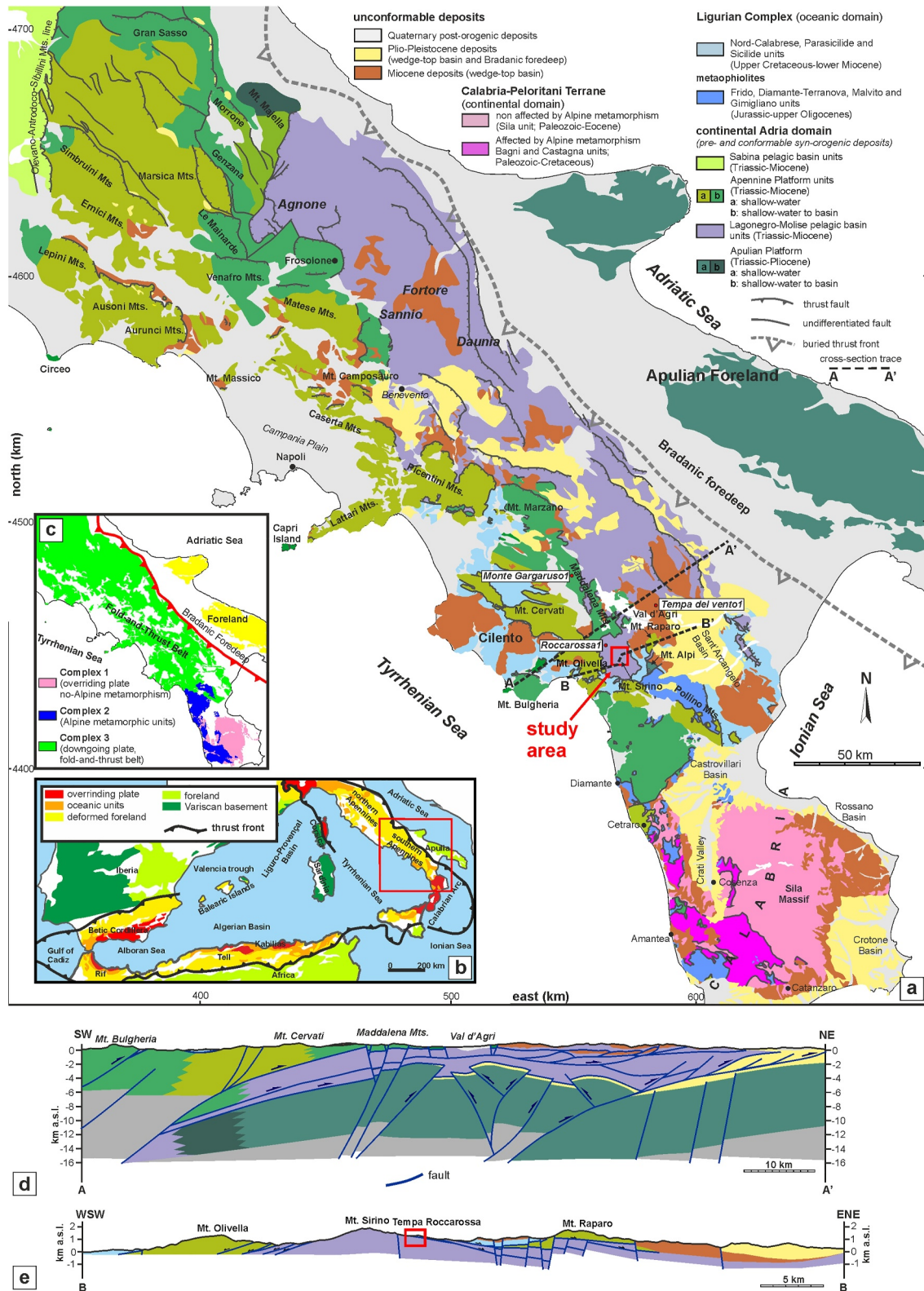


Figure 1. (a) Geological map of the northern Calabria-southern Apennines System (modified after Vitale & Ciarcia, 2022). (b) Tectonic sketch of western-central Mediterranean Alpine belts (modified after Vitale et al., 2015). (c) Map of the orogenic complexes of the Apennines. (d) A-A' geological cross-section (modified after Mazzoli et al., 2013). (e) B-B' geological cross-section including the studied area.

extension shifted from W to E, affecting the chain with the formation of several coastal and intramontane plains, accompanied by volcanism (e.g., Fernandez et al., 2025; Santangelo et al., 2017). The deep structure of the southern Apennines (Figure 1d) consists of the superposition of the allochthonous wedge made of LAC, ApeP and LMB thrust sheets on a para-allochthonous wedge, corresponding to the buried and shortened ApuP succession.

2.1. Tempa Roccarossa Area

The study area of Tempa Roccarossa is located in the Basilicata region along the northeastern slope of Mt. Sirino (Figure 1e), a large anticline composed of LMB units underlain by ApeP and the LAC through low-angle normal faults (e.g., Mazzoli et al., 2006). The Tempa Roccarossa area has been mapped by the Servizio Geologico d'Italia (1969) and ISPRA (2014). Here, the tectonic architecture is defined by the superposition of two main LMB thrust sheets. The succession forming the backbone of the Mt. Sirino (lower LMB unit or Lagonegro I unit of Scandone et al., 1967) is composed of Jurassic-Lower Cretaceous pelagic basin sedimentary units including cherty carbonates (*Calcari con Selce* Formation), radiolarites and silicified limestones and argillites (*Scisti Silicei* Formation), and silicified argillites (*Flysch Galestrino* Formation; Ciarapica & Passeri, 2000; ISPRA, 2014). This succession is tectonically covered by another LMB thrust sheet (upper LMB unit or Lagonegro II unit of Scandone et al., 1967; Figures 2a, 2b, and 2f), which includes at the base a Triassic succession of reefal bodies embedded in argillites, silts, radiolarites and sandstones (*Monte Facito* Formation; Ciarapica & Passeri, 2000; ISPRA, 2014).

2.2. Tectonic Mélange

In the southern Apennines, the term “tectonic mélange” usually refers to highly deformed rocks exposed in a few outcrops and drilled at depth for oil exploration (Corrado et al., 2002; Mazzoli et al., 2006; also called “Irpianian units” in several well-logs, ViDEPi Project, 2025). These rocks are set between allochthonous LMB units and between LMB and the ApuP units (Figure 1d; Ascione et al., 2013; Butler et al., 2004; Catalano et al., 2004; Corrado et al., 2002; Mazzoli, 1992; Mazzoli, Barkham, et al., 2001; Mazzoli, Zampetti, & Zuppetta, 2001; Rinaldi et al., 2020; Schirripa Spagnolo et al., 2024). Borehole data indicate a maximum thickness of a few hundred meters and a succession formed by intensely deformed shales and siltstones, with exotic fragments of sandstones and limestones. Cuttings from well logs show that the mélange results from the fragmentation of LMB and ApeP successions. The mélange is also exposed in different localities (Catalano et al., 2007; Ciarapica & Passeri, 2000; Corrado et al., 2002; Mazzoli et al., 2006; Passeri & Ciarapica, 2010; Van Dijk et al., 2000), including the area between Mt. Alpi, Mt. Sirino (Tempa Roccarossa) and Sasso di Castalda (Figure 1a).

At Mt. Alpi, the mélange is tectonically juxtaposed to the upper Messinian clastic unit (*conglomerati ed arenarie di Cima S. Croce* Formation; “Lauria” sheet; ISPRA, 2014) at the top of the ApuP succession and to the base of the LMB thrust sheet. The Messinian succession consists of flattened polygenic conglomerates, sandstones with carbonate cement, and shales with subordinate sandstones from the bottom to the top. The tectonic mélange is composed of a heavily deformed argillaceous silty matrix, including black-brown, red, and green pelites with blocks of calcareous sandstones, micritic limestones, radiolarian cherts, laminated black algal limestones, and calcarenites (Alberti et al., 2001; Mazzoli et al., 2006; Van Dijk et al., 2000). In other localities, the mélange is embedded between LMB thrust sheets and is typically located at the base of the Lower Triassic *Monte Facito* Formation (Cavalcante et al., 2023; Ciarapica & Passeri, 2000; Passeri & Ciarapica, 2010).

The analyzed tectonic mélange crops out at Tempa Roccarossa, east of Mt. Sirino (Figures 2a and 2f). The latter is a 20 km-sized, dome-shaped anticlinal structure characterized by the interference of two sets of folds and thrusts, the first verging to NE/E/SE and the second to N (Mazzoli, 1992, 1995). The analyzed mélange is located at the base of the upper LMB unit, at the contact with the underlying lower LMB unit (Figures 2c, 2d, and 2f). Information about the deep structure of the area comes from the available well logs of *Roccarossal*, *Tempa del Vento1* and *Monte Gargaruso1* (Figure 1; ViDEPI Project, 2025). In particular, the *Roccarossal* well is located close to the study area (Figure 1a). The reconstructed stratigraphic logs (Figure 2e) reveal a structure characterized by the mélange located above the Apulian carbonates, and embedded between two LMB thrust sheets, the latter corresponding to the exposed section of the study area.

Mazzoli (1992) described the Tempa Roccarossa mélange, associated with a regional shear zone, as highly deformed chlorite claystones characterized by rotated porphyroclasts and shear bands, indicating a mean tectonic transport to NE. The Author reconstructed two deformation phases, the first (D_1) responsible for forming

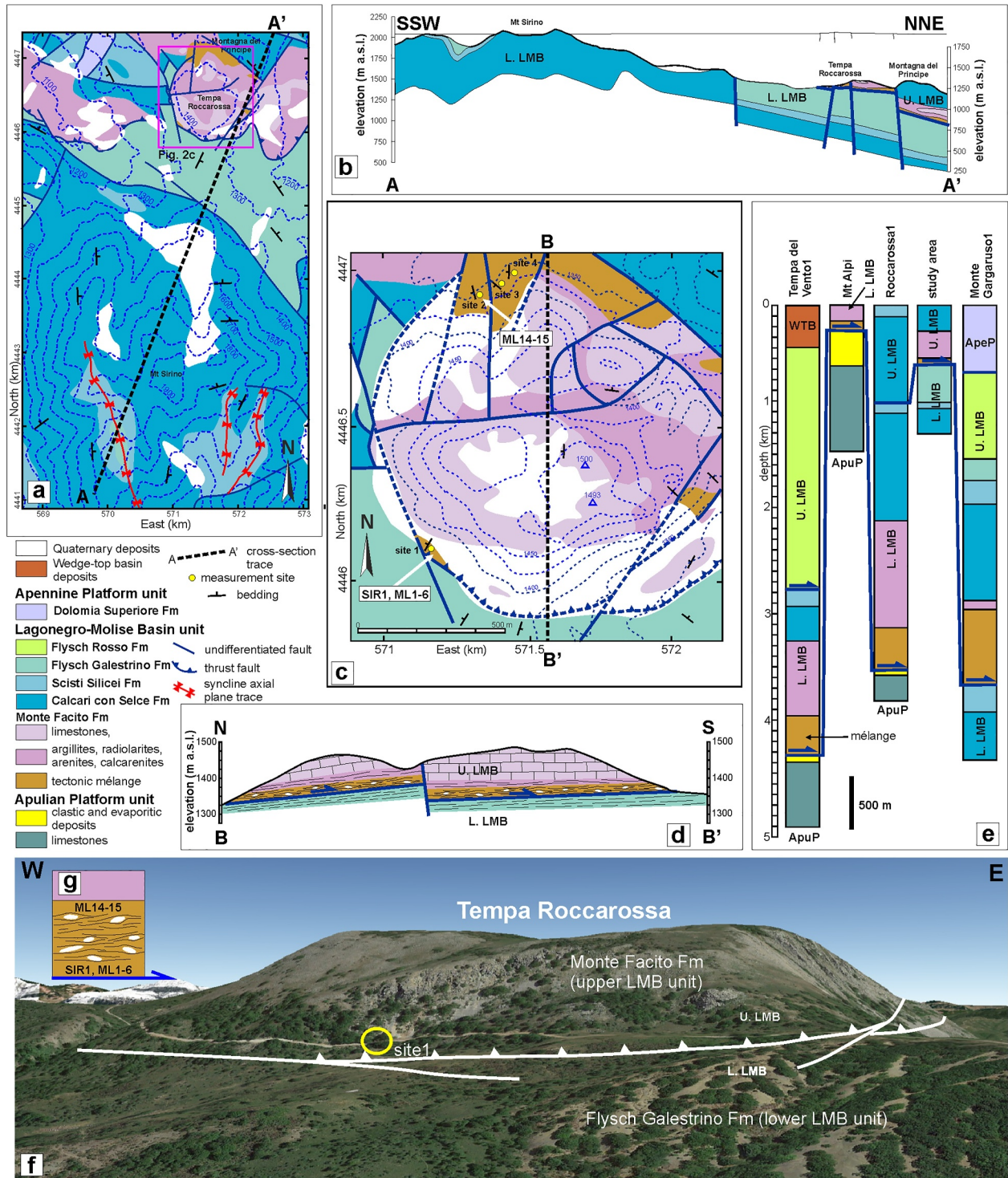


Figure 2. (a) Geological map of Mt. Sirino (modified after ISPRA, 2014). (b) Geological cross-section A-A'. (c) Geological map of Tempa Roccarossa (modified after Ciarapica & Passeri, 2000). (d) Geological cross-section B-B' (modified after ISPRA, 2014). (e) Schematic well logs (modified after ViDEPi Project, 2025). The locations of the wells are shown in Figure 1a. UTM projection, zone 33, datum WGS84. (f) Panoramic view of Tempa Roccarossa. L. LMB and U. LMB: Lower and upper Lagonegro-Molise Basin units, respectively.

a main foliation, and a second phase (D_2) characterized by structures folding the previous foliation. Catalano et al. (2007) studied some outcrops of the LMB unit, including the Tempa Roccarossa mélangé, and reconstructed a polyphase deformation evolution. They show the development of a main foliation (S_1) associated with the formation of the tectonic mélangé (stage D_1) defined by a preferred orientation of platy minerals with associated intrafolial folds. These structures are deformed by millimeter to centimeter folds (stage D_2) with NE–SW trending axes producing a crenulation cleavage (S_2). In addition, D_1 and D_2 structures are deformed by decimetric to metric thick shear zones (stage D_3) that form an S–C fabric, producing an anastomosed pattern formed by lenticular microlithons bounded by shear planes. Kinematic indicators define a top to the NE direction of shear. The latest shortening structures are NW–SE trending conjugate thrust faults with associated asymmetric folds (stage D_4). The Authors also determined the temperature estimate using the Kubler Index in the samples from the *Monte Facito* Formation collected at several locations, including the Tempa Roccarossa locality. Their results suggest a maximum temperature range of 220–250°C and a burial depth of 8–9 km. However, contrary to Mazzoli (1992), the Authors associate the mélangé with a shear zone located between LMB units and overlying ApeP units.

3. Materials and Methods

In the Tempa Roccarossa study area, we collected several samples from Site 1 (Figure 2c; SIR1, ML1–6; Table S1 in Supporting Information S1) close to the main thrust fault. They are characterized by calcareous and quartzose clasts, less than a few centimeters in size, embedded in a well-foliated argillitic matrix. In Site 2, located at a distance from the thrust, we collected two samples (ML14, 15; Table S1 in Supporting Information S1). These rocks are defined by a few clasts and a dominant argillitic matrix with a weak foliation. Twenty subsamples were taken from the sample SIR1 and ML1–6 to obtain thin sections and polished slabs for the structural and petrographic characterization parallel to the XZ, YZ, and XY planes of the Finite Strain Ellipsoid (FSE). As explained in the following paragraphs, the analyzed samples are S-tectonites, characterized by oblate strain, and are defined by a dominant tectonic foliation, with stretching lineations being rare or absent. Therefore, to evaluate the X, Y, and Z axes of the FSE, we considered other features such as synthetic and antithetic S–C' structures (R_1 and R_2 , respectively) and rotated porphyroclasts. The results indicate that the XZ is defined by an NW–SE direction (shear direction) with the XY plane approximately horizontal. We then cut samples orthogonal to the main foliation (XY plane) and parallel and orthogonal to the shear direction (NW–SE). In total, we obtained 13 thin sections (ML1a, 2a, b, 3a, 4, 5, 6a, b) cut parallel to the XZ plane and six (ML1b, c, 2c, 3b, c, 6c) cut parallel to the YZ plane, and one (SIR1) cut parallel to the XY plane.

3.1. Mineralogical, Mineral Chemical and Whole-Rock Geochemical Analyses

Mineralogical XRPD (X-Ray Powder Diffraction), mineral chemical SEM-EDS (Scanning Electron Microscopy Energy Dispersive Spectrometry) and whole-rock geochemical XRF (X-Ray Fluorescence Spectrometry) analyses were performed on a selection of five representative samples (SIR1, ML1, 2, 14, 15; Table S1 in Supporting Information S1). Two additional samples (ML3, 6; Table S1 in Supporting Information S1) were analyzed only for mineral chemical SEM-EDS characterization.

3.1.1. XRPD Analysis

XRPD analysis was performed to identify and quantify mineral phases. Samples were dried at room temperature, gently crushed, homogenized, and split into two aliquots. One portion was grinded for both XRPD and XRF analyses, while the other was used for wet extraction of clay fractions ($<2\ \mu\text{m}$) following Stock's law (Moore & Reynolds, 1997). A Philips X'Pert Pro instrument, with Bragg Brentano geometry, equipped with a Co anode (setting 40 kV and 40 mA) and X'Celerator detector housed at the *Dipartimento di Geoscienze* of the *Università di Padova* was used. The data were collected using a spinner sample holder, with a 2θ angle ranging from 3° to 85° , for both random powder bulk samples and oriented specimens of the clay fraction. The random powder of the bulk sample was prepared using the side-loading method (Srodon et al., 2001). Oriented specimens of the clay fraction were prepared by settling a suspension after being saturated with Mg^{++} cations using 1 N MgCl_2 solution. Each specimen was analyzed, air-dried, glycolated at 60°C for 8 hr and heated at 375°C for 1 hr (Moore & Reynolds, 1997). Quantitative analysis was carried out on bulk sample XRD profiles measuring the peak area of both phyllosilicates and non-phyllosilicates (Cavalcante et al., 2007) using the Winfit software (Krumm, 1999) for the decomposition of peaks, the determination of integrated intensity, and the measurement of peak height and Full

Width at Half Maximum (FWHM). Results were compared with whole-rock major oxides data using the experimental software vbAffina (Cesarano et al., 2018; Leoni et al., 2008). A semi-quantitative analysis of clay minerals amount in clay fraction was performed on glycolated and heated XRD patterns (Cavalcante et al., 2007). The paleotemperatures were determined by the Kübler Index (KI) using the international standards proposed by Warr and Rice (1994), recalibrated with KI values provided by M. Frey and W.B. Stern (University of Basel) (Warr & Ferreiro Mählmann, 2015). In particular, the temperatures were estimated using the diagram (KI vs. T) reported by Cavalcante et al. (2012). This diagram was reconstructed considering the KI value and temperature from the literature (see Cavalcante et al., 2012 and references therein). The average error percentage for FWHM measurements is about 6% (Warr, 2018), corresponding to a temperature range of $\pm 10^{\circ}\text{C}$.

3.1.2. XRF Analysis

For XRF analyses, powdered rock samples were used to prepare pressed powder pellets, which were analyzed for major oxides and trace elements using a Panalytical Axios instrument housed at the DiSTAR. Analytical uncertainties are in the order of 1%–2% for major oxides and 5%–10% for trace elements. Weight loss on ignition (LOI) was determined gravimetrically after heating 1 g of rock powder (pre-dried at $\sim 150^{\circ}\text{C}$ overnight) at 900°C for three h. Full results and quality control data are reported in Supporting Information S2 as Tables S2.1–S2.4.

3.1.3. SEM-EDS Microanalysis

The SEM-EDS microanalyses were carried out at the DiSTAR using an Oxford Instruments Microanalysis Unit equipped on a Zeiss Merlin VP Compact Field Emission SEM. The technique has been demonstrated to provide reliable microanalytical data at the major oxides concentration levels (see Guyett et al., 2024 and references therein). Measurements were performed using a 15-kV primary beam voltage, 60 μA filament current, variable spot sizes and a 10-s of acquisition time. Corrections for matrix effects were performed using the XPP correction routine based on a Phi-RoZeta approach. Standards for calibration were: anorthoclase (Na, Al, Si); microcline (K); serandite (Mn); diopside (Ca); fayalite (Fe); olivine (Mg); rutile (Ti); apatite (P); fluorite (F); barite (Ba); celestine (Sr); zircon (Zr and Hf); synthetic Smithsonian orthophosphates (La, Ce, Nd, Sm, Y and Sc); pure niobium (Nb); pure vanadium (V); pure cobalt (Co); pure nickel (Ni); chromite (Cr); Corning glass (Th and U); sphalerite (Zn); pyrite (S); sodium chloride (Cl); pollucite (Cs). Accuracy and precision were tested using the rhyolitic Lipari obsidian ID3506 and basaltic Laki 1783 tephra from Kuehn et al. (2011) as secondary standards. Relative analytical uncertainty was $<5\%$ for SiO_2 , Al_2O_3 , K_2O , CaO , and FeO , $\sim 10\%$ for the other elements.

3.2. Chlorite and White Mica Multi-Equilibrium Geothermobarometry

A multi-equilibrium approach was used to determine the P and T conditions for forming chlorite and white mica. The chlorite + quartz + H_2O method of Vidal et al. (2005, 2006) was used to estimate the formation temperature of chlorite. Assuming that the maximum temperatures represent the conditions of peak metamorphism (e.g., Lanari et al., 2012; Petroccia et al., 2025), the pressure conditions of white mica formation were determined using the mica + quartz + H_2O method of Dubacq et al. (2010). Finally, a P-T estimate was obtained using the chlorite + mica + quartz + H_2O method of Vidal et al. (2006). Chlorite and white mica analyses have been selected where the equilibria show good convergence in the P-T space, but this is not sufficient to prove chemical equilibrium; it only shows that the mineral composition is consistent with chemical equilibrium being achieved at these P-T conditions (Lanari & Duesterhoeft, 2019). A full description of each method and the limitations of this approach compared to others can be found in Lanari and Duesterhoeft (2019) and Petroccia et al. (2025). Thermodynamic calculations were performed using the ChlMicaEqui 1.5 program (Lanari, 2012; Lanari & Duesterhoeft, 2019). The following solution models were used: Vidal et al. (2005, 2006) for chlorite (chlorite + quartz + H_2O and chlorite + mica + quartz + H_2O methods), Parra et al. (2002) for white mica (chlorite + mica + quartz + H_2O method) and Dubacq et al. (2010) for the determination of a P-T line along which mica is in equilibrium with quartz and H_2O (mica + quartz + H_2O method). All solution models are compatible with the equations of state and the internally consistent data set of Berman (1988). The activity of H_2O in the fluid was set to 1.

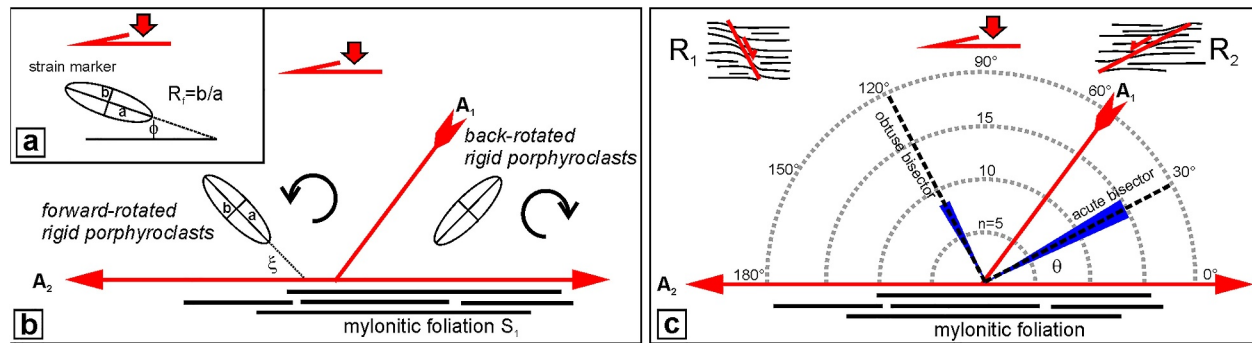


Figure 3. (a) R_f/ϕ method for strain analysis. Vorticity W_k estimation: (b) rigid porphyroclast method; (c) synthetic and antithetic S-C' structures (R_1 - R_2) method. See the text for details.

3.3. Strain and Structural Analysis

To obtain information about the strain in 3D, we reconstructed the FSEs for four samples (ML1, 2, 3, 6). Using the R_f/ϕ method (Figure 3a; Ramsay, 1967; Dunnet, 1969), we analyzed the strain markers with the free software EllipseFit (Vollmer, 2018). The technique uses strain markers that can be approximated to ellipses by measuring their ellipticity (R_f) and the angle ϕ that the long axis of the ellipse forms with a reference line (Figure 3a). We considered only the objects deformed by ductile strain for the finite strain estimation, that is, the calcareous clasts, and avoided the rigid porphyroclasts, that is, the quartz clasts, on the contrary characterized by brittle deformation, which would furnish an underestimation of the finite strain (Vitale, Tramparulo, et al., 2020). Another assumption is that the long axes of the original objects were randomly oriented before the ductile deformation (Dunnet, 1969). The main limitations of this method are the preparation of the slabs and thin sections, especially the choice of the XZ and YZ planes. In addition, another uncertainty arises in the case of a preferred orientation recorded before the ductile deformation. Finally, the FSEs were classified using the Flinn-Ramsay plot (Flinn, 1962; Ramsay & Huber, 1983). Fault planes, lineations, fold axes, and axial planes were analyzed by OpenStereo free software (Grohmann & Campanha, 2010).

3.4. Kinematic Vorticity Analysis

To obtain information about the degree of coaxial strain, we estimated the kinematic vorticity W_k using two different methods. The dimensionless number W_k indicates the partitioning between a coaxial and non-coaxial deformation (Means et al., 1980), varying between 0 (pure shear) and 1 (simple shear). Intermediate values indicate the coexistence of pure and simple shear (general shear, Means & Park, 1994; Tikoff & Fossen, 1995; or sub-simple shear, Fossen & Cavalcante, 2017). The first of the methods employed for W_k determination (Figure 3b) is based on the evidence that in a general shear, rigid objects can rotate forward or backward with respect to the sense of shear (Jessup et al., 2007; Wallis et al., 1993). However, all porphyroclasts are further partitioned into two populations: one rotates continuously without developing a preferred orientation, and the other aligns along a minimum energy position (Jessup et al., 2007). We calculated the vorticity number W_k using the Rigid Grain Net (RGN), which includes a series of semi-hyperbolas that allow a simple estimation of this kinematic parameter. The method (Figure 3b) uses the estimation of the angle ξ that the long axis forms with the mylonitic foliation and the factor B^* attained by the following equation:

$$B^* = \frac{a^2 - b^2}{a^2 + b^2},$$

where a and b are the long and short axes of the rigid object, respectively.

The second method for evaluating the W_k uses synthetic (R_2) and antithetic (R_1) S-C' structures (Behrmann, 1987; Grasemann & Stüwe, 2001; Platt & Vissers, 1980), which are very common features in general shear zones (Xypolias, 2010). This method (Gillam et al., 2013; Kurz & Northrup, 2008) is based on the orientation of R_1 and R_2 planes with respect to the shear zone boundary. Generally, R_2 shear planes are oriented parallel to the acute bisector of the flow apophyses (A_1 and A_2 , Figure 3c) or at a lesser angle (Kurz & Northrup, 2008), whereas

R_1 shear planes are poorly developed and have a mean inclination parallel to the obtuse bisector of the flow apophyses. The vorticity number is calculated by the equation (Kurz & Northrup, 2008) $Wk = \cos(2\theta)$, where θ is the angle between R_2 and the shear plane assumed to be parallel to the flow apophysis A_2 (Gillam et al., 2013; Kurz & Northrup, 2008), hence parallel to the mylonitic foliation in highly deformed shear zones.

The two methods are independent approaches that use two different types of structures. Both depend on the amount of simple and pure shear and can, therefore, provide independent estimates. However, both methods have some limitations, including the three-dimensional problem, that is, we have studied the motion of rigid clasts in two-dimensional sections that are only projections in the plane of the thin section (e.g., Iacopini et al., 2011; Montemagni et al., 2020). As in the sample preparation for the strain analysis, the sample cuts may not be perfectly parallel to the XZ plane of the FSE and hence furnish underestimations of the dip angle of R_1 and R_2 planes and the contribution of the pure shear. Furthermore, for the S-C' method, some R_1 and R_2 planes may be influenced by rigid porphyroclasts modifying the dip values. To overcome the latter limitation and reduce uncertainty, we calculated the mean dip angles using a frequency distribution that is approximately Gaussian. For individual Wk values, we adopted an uncertainty of ± 0.1 , as indicated by Tikoff and Fossen (1995), which are values greater than 0.8 (Iacopini et al., 2011). In any case, using both methods allows us to identify more realistic value intervals.

We analyzed the thin sections of samples ML1, 2, 3, and 6 and the polished slab of ML1 by the RGN method, obtaining 174, 202, 136, and 165 data for samples ML1, 2, 3, and 6, respectively. The R_1 - R_2 method was applied to the same samples, collecting 282, 276, 348, and 218 data for samples ML1, 2, 3, and 6, respectively.

4. Results

4.1. Mesostructures

We studied four outcrops in the Tempa Roccarossa mélangé (Sites 1 to 4 in Figure 2c). Site 1 hosts the most deformed rocks, located near the main thrust contact, close to the underlying *Flysch Galestrino* Formation located in the footwall. In contrast, the other three sites are more distant from it and generally appear as less deformed rocks. In general, the tectonic mélangé appears as a well-foliated rock with clasts embedded in a very fine-grained matrix (Figure 4).

We recognized three foliations at the outcrop scale: the bedding (S_0) and two superimposed tectonic cleavages, S_1 and S_2 . The latter is the main foliation. Rare mesoscale F_1 folds are present (Figure 4a), deforming the S_0 bedding, generally with a rounded hinge, overturned and with narrow to isoclinal geometries and NW-SE trending axes, parallel to tectonic transport. Along the limbs, an S_1/S_2 cleavage is observed (Figure 4a). To the naked eye, clasts embedded in the main foliation vary in size from a few centimeters to <1 mm (Figures 4b–4g). The largest clasts often have a rectangular shape, commonly rotated, and, in places, show the bedding S_0 (Figures 4b–4g) and, in some cases, the first tectonic foliation S_1 (Figures 4c, 4e, and 4g). The latter corresponds to a stylolitic cleavage in the calcareous clasts (Figure 4c) and forms a high angle with the bedding.

At Site 2 (Figure 2c), the mélangé shows a less intense deformation. In fact, locally, remnants of the protolith formed by dismembered calcareous or arenaceous layers alternate with fine-grained layers (Figure 4h). The S_1/S_2 foliation is parallel to the original S_0 bedding, as indicated by the alternating purple/green colors.

Locally, the S_2 is affected by microscale folding, marked by a crenulation lineation (L_3) with a subhorizontal NE-SW trend (Figure 4i). Furthermore, the S_2 foliation is cut by two sets of normal shear planes, set 1 (R_1) forming high angle planes with the main foliation and set 2 (R_2) with a lower angle (Figures 4j and 4k). In general, planes R_1 and R_2 dip to the NW and SE, respectively, as indicated by the stereographic projection (Figure 4j). Sites 3 and 4 are similar, showing a lower amount of porphyroclasts and a parallel main foliation (S_2) cut only by the R_1 and R_2 shear planes (Figure 4j).

4.2. Microstructures

Polished slabs of mélangé samples (Figure 5a) exhibit a mylonite fabric, characterized by deformed porphyroclasts enclosed within a highly foliated fine matrix. Clasts are affected by ductile strain, frequently displaying an elliptical shape. Thin sections exhibit up to three distinct foliations (Figures 5b–5o). S_0 is observed only in the rigid porphyroclasts (Figures 4b–4g).

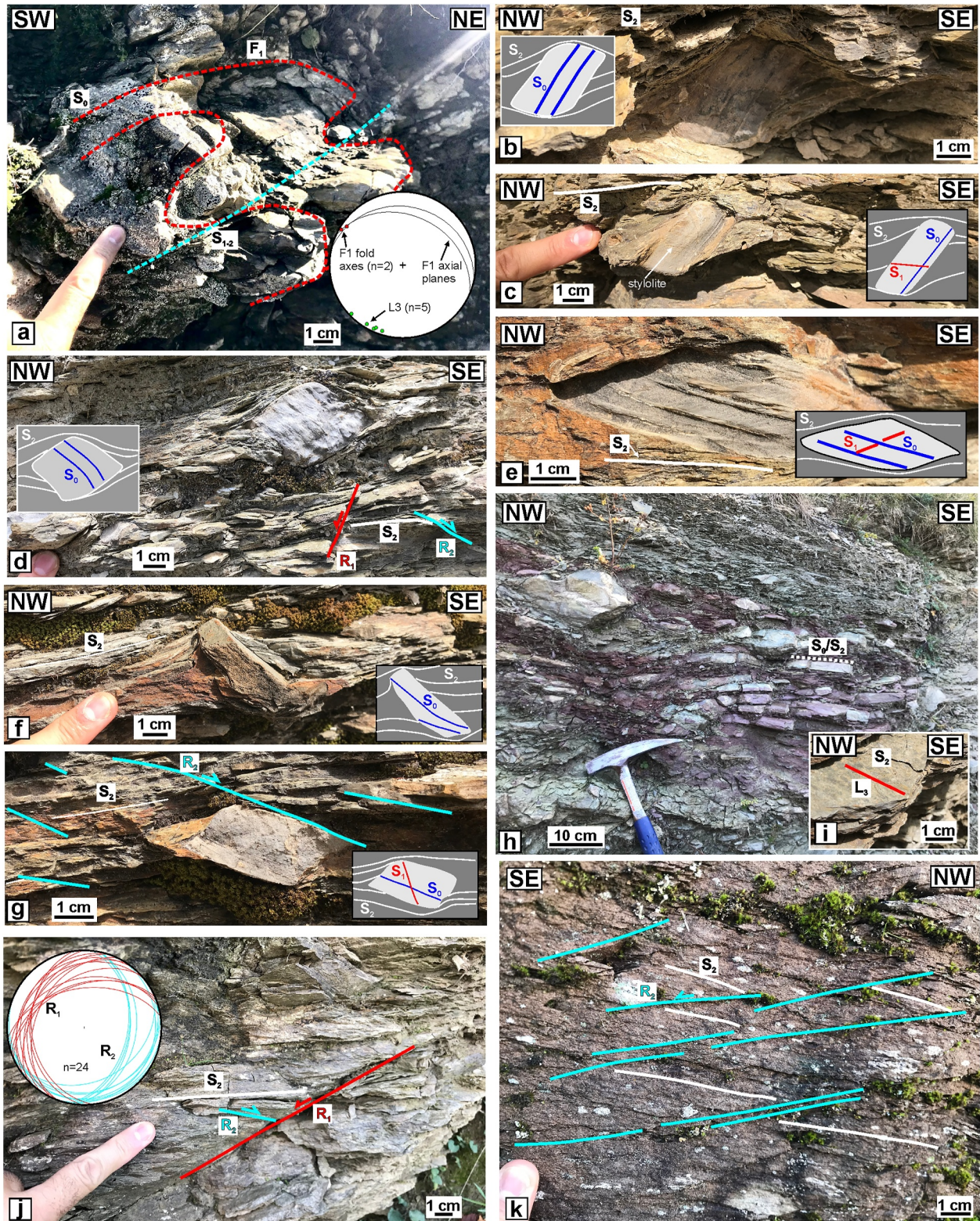


Figure 4. Representative field photographs of the Tempa Roccarossa study area showing (a) F1 isoclinal folds (Site 2); (b–g) rotated clasts embedded in a foliated matrix with R_1 and R_2 shear planes (Site 1); (h) remnants of the original bedding (Site 2), (i) lineation L_2 on the S_2 foliation (Site 1); (j) R_1 and R_2 shear planes and related stereographic projection (Site 3), (k) R_2 shear planes (Site 4). Site locations are shown on Figure 2c.

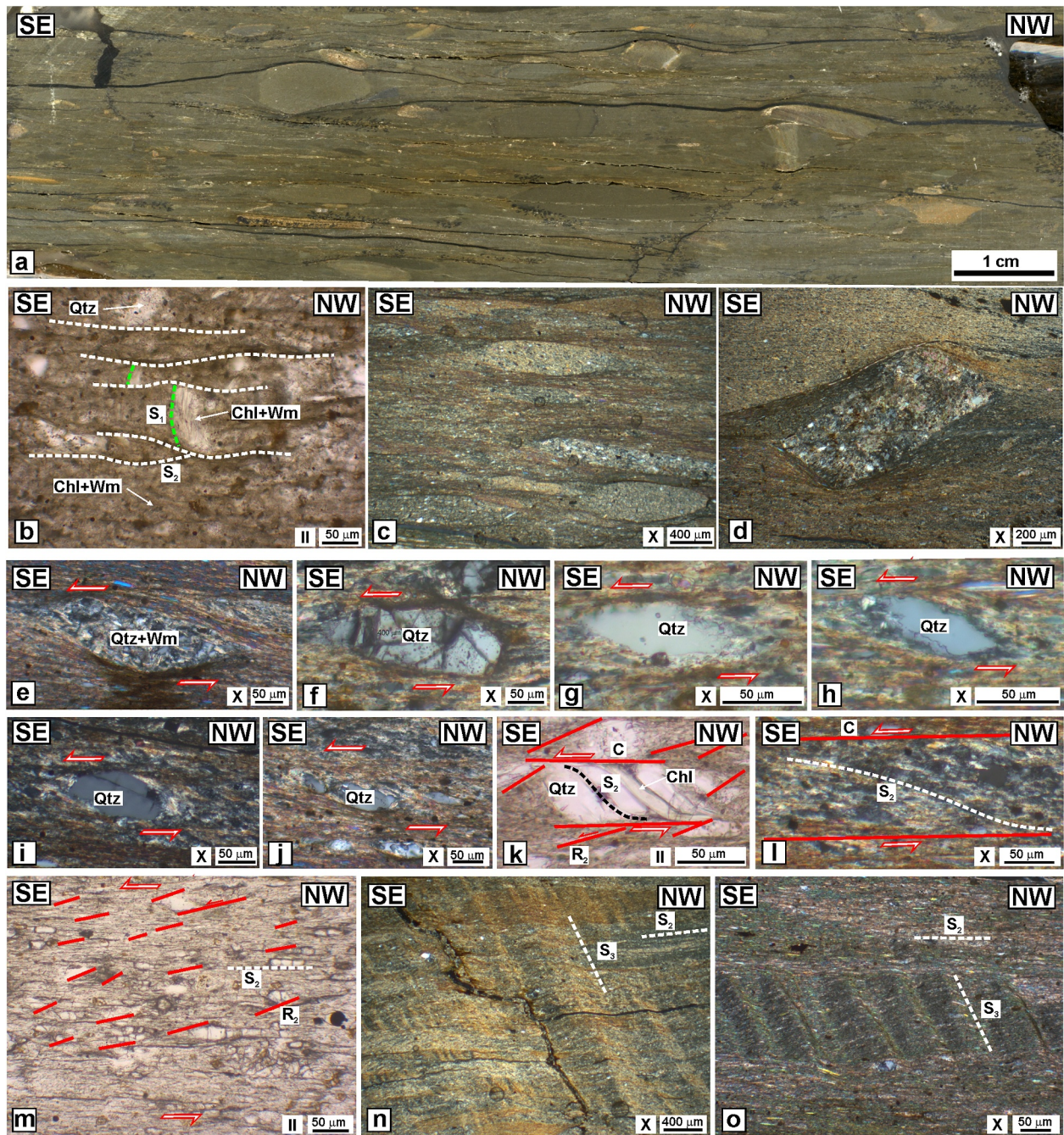


Figure 5. Representative microstructures for the investigated Tempa Roccarossa mélangé samples, observed on polished thin slab (a) and in thin section photomicrographs (b–o, II for plane polarized, X for crossed polarizers light views). (a) Sample ML1 cut along the SE–NW direction showing rotated rigid porphyroclasts and elliptical markers affected by ductile strain. (b) S_1 and S_2 cleavages (sample ML2; Qtz, Chl and Wm for quartz, chlorite and white mica crystals, respectively). (c) Elliptical strain marker (sample ML2). (d) Rotated rectangular porphyroclast (sample ML2). (e–h) S–C structures and porphyroclasts with a sigma shape (sample ML6a). (i–m) R_2 shear planes (synthetic S–C' structures) (sample ML3). (n–o) Late cleavage (S_3) superposing on main foliation (S_2) (sample ML2).

The earliest deformation structure is a cataclasite attached to the porphyroclasts (Figure 6h) made of rounded fragments of the porphyroclast or by an older cataclasite. Porphyroclasts (Figures 5c–5k) are made of elliptical fine-grained objects (Figure 5c), large rectangular coarser quartz and calcite grains (Figures 5d and 5e) or fragments of calcite veins. Small rigid porphyroclasts are generally made of fractured (Figure 5f) or single quartz crystals (Figures 5g–5i). Frequently, they show a monoclinical symmetry forming σ shapes (e.g., Passchier & Trouw, 2005).

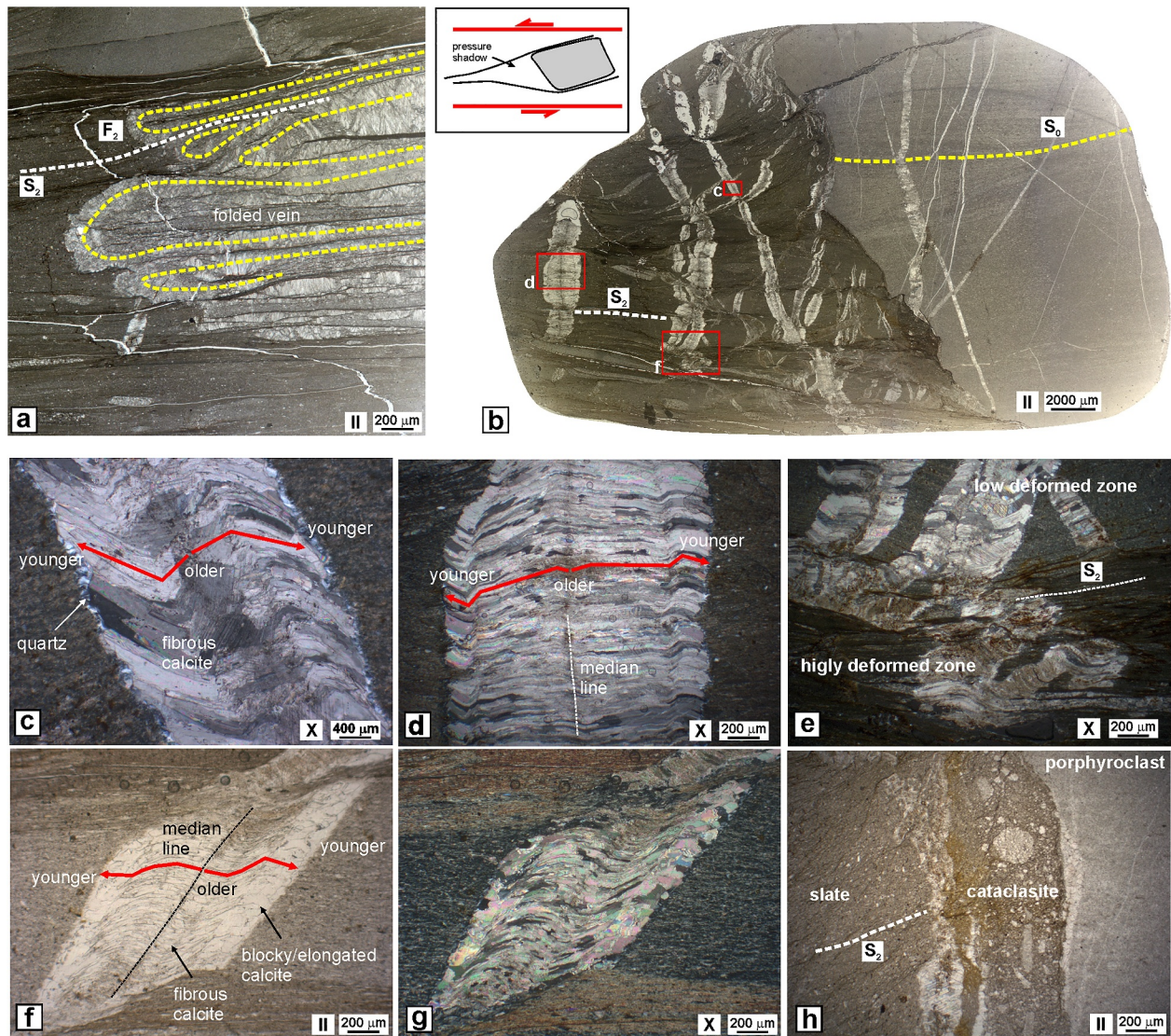


Figure 6. Representative microstructures for the investigated Tempa Roccarossa mélange samples, observed in thin sections (II for plane polarized, X for crossed polarized light views). (a) Folded early vein (ML6a). (b) Veins located in a pressure shadow of a rotated porphyroclast (ML6a). (c–e) Close-up view of some veins of picture (b): (c) antitaxial vein with sigmoidal growth of calcite fibers and quartz cement at the boundaries; (d) fibrous vein with a median line; (e) deformed early vein; (f–g) Antitaxial vein in the neck of a stretched layer (ML6b). (h) Remnant of cataclasite in a pressure shadow of a porphyroclast (ML6b).

As depicted in Figure 5b, the tectonic foliation associated with a first deformation stage (D_1) is a disjunctive cleavage S_1 occurring in microlithons of main foliation S_2 . S_1 is characterized by alternations of chlorite and mica crystals. Some veins associated with stage D_1 are well-preserved in the strain shadow of large porphyroclasts (Figures 6b–6e). These veins are made of calcite fibers departing from the median line (antitaxial veins), with the youngest generations located to the boundaries, where quartz crystals are often present (Figure 6c). The fibers show a sigmoidal shape (Figure 6c) or a complex geometry (Figure 6d). Locally, early antitaxial veins occur at the necks of boudinaged layers showing the same fibrous sigmoidal growth and quartz cement at the boundaries (Figures 6f and 6g). At the boundary of the pressure shadow, the veins are deformed by ductile shear (Figure 6e) and isoclinally folded with limbs parallel to the main foliation S_2 (Figure 6a).

As shown in Figure 5b, the latter is a crenulation cleavage that is always defined by chlorites and micas, which generally mantle the porphyroclasts (Figures 5c–5k). S_2 cleavage is deformed by S-C (R_1) and S-C' (R_2) structures (Figures 5j–5m) and, especially in the very fine-grained parts, is deformed by kink folds, whose axial

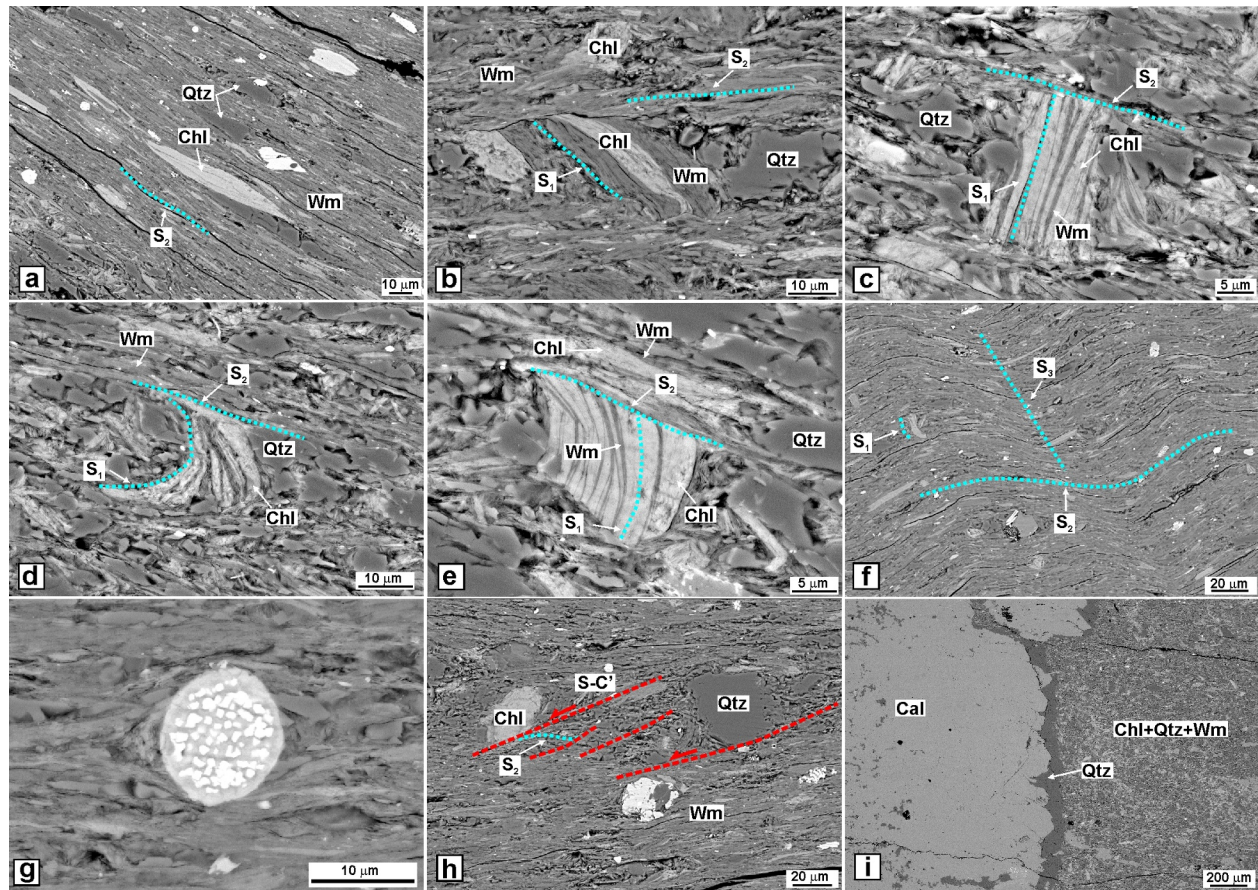


Figure 7. Representative back-scattered electron SEM images for the investigated Tempa Roccarossa mélangé samples. (a) Highly deformed area, showing the main foliation (S_2) marked by the iso-orientation of white mica (Wm), chlorite (Chl), and elongated quartz (Qtz) (ML6). (b–e) Examples of relicts of S_1 foliation in microlithons marked by Wm and Chl crystals: (b) ML2; (c–e) ML6a. (f) Relict S_1 foliation in microlithons, the main foliation S_2 and a new, early S_3 crenulation foliation (ML2b). (g) Pre-kinematic grain of pyrite crystals (white) in iron hydroxide (light gray) embedded by Wm (ML2). (h) R_2 shear planes (ML2). (i) Boundary between the pelitic Chl + Wm + Qtz matrix and a syn-kinematic antitaxial vein of Qtz and calcite (Cal; ML6a).

planes form a cleavage S_3 (Figures 5n and 5o). σ -shaped porphyroclasts, S-C structures invariably indicate top-to-the-E/SE shear sense.

SEM investigations revealed that a disjunctive cleavage (S_1) is deformed by a main crenulation cleavage (S_2) that partially or totally transposes previous structures. In the highly deformed zones (Figure 7a), only the main foliation (S_2) marked by the orientation of white mica, chlorite, elongated quartz, rutile, and apatite crystals is observed. In the lower deformed areas, relicts of S_1 foliation are preserved in microlithons (Figures 7b–7f). The S_1 is a disjunctive cleavage marked by the alternation of white mica and chlorite crystals, which are occasionally folded (Figures 7d and 7e). Locally, the main foliation S_2 is crenulated (Figure 7f) with a less developed new foliation S_3 . Porphyroclasts and porphyroblasts, made of chlorite, quartz, rutile and pyrite, are also observed (Figure 7g). Generally, micro-shear planes R_1 and R_2 occur (Figure 7h). Finally, syn-kinematic antitaxial veins show quartz as the last growth at their boundaries (Figure 7i).

4.3. Petrographic Description

The samples investigated are extremely fine-grained and display a weakly-to-developed main foliation (S_2) in thin sections. They all comprise a mineral assemblage dominated by white mica (Wm) and chlorite (Chl) crystals. Sporadic porphyroclasts of quartz (Qtz), albite and calcite, accessory apatite, rutile, zircon, pyrite, and Fe-hydroxides (identified during SEM observations) also occur, as well as veins of quartz and/or calcite.

A textural distinction is tentatively made between samples showing a more evident foliation (ML1,2,3,6 and SIR1) and samples showing a very weak foliation (ML14, 15). For the sake of simplicity, in the following sections, the two sample types will be referred to as “slate” and “metapelite,” respectively.

4.3.1. Mineralogical Data

The quantitative mineralogical analysis shows that the bulk rock is mainly characterized by the presence of phyllosilicates ranging from 56% to 72%, subordinately quartz (from 14% to 30%) and feldspars (i.e., alkali feldspar + plagioclase) in some percentage units (from 3% to 4%). Calcite is absent in the metapelite sample ML14, whereas in the slate ML2 sample, it reaches 27% (Tables S2.1–S2.4 in Supporting Information S2; Bulk sample). Hematite is present in a few percentages only in metapelite sample ML15. Phyllosilicates consist of illite-muscovite (36–43 wt.%), chlorite plus mixed-layers chlorite/smectite (C/S) (17–24 wt.%). Paragonite (plus K/Na mica) is present in very low amounts (3%–6%) in SIR1, ML1 and ML2 samples (Tables S2.1–S2.4 in Supporting Information S2; Figure 8).

The semi-quantitative mineralogical analysis of the clay fraction shows the main presence of illite-muscovite and chlorite. Mixed layers of chlorite/smectite (C/S) are detectable in lower amounts, while paragonite plus K/Na mica is slightly higher, especially in the slate samples (Tables S2.1–S2.4 in Supporting Information S2; Figure 8). KI value varies from 0.42 in the metapelite sample ML14 to 0.31° 2 Θ in slate SIR 1. Intermediate values are measured in samples ML1, ML2, and ML15. This suggests that metapelite samples (Site 2) were subjected to a less pronounced metamorphic recrystallization than slate ones (Site 1). Therefore, differences in the KI between ML14 and ML15 are due to different textural and/or chemical compositions of the original protolith. In summary, the KI indicates that the paleotemperatures vary between about 200 \pm 10°C (ML14) and 250 \pm 10°C (SIR 1). This agrees with the presence of paragonite and the very low amount of C/S (Tables S2.1–S2.4 in Supporting Information S2; Figure 8) (Cavalcante et al., 2012; Kisch, 1987; Leoni et al., 1996).

4.3.2. Mineral Chemistry

4.3.2.1. Chlorite (Chl)

Chl crystals are generally larger compared to Wm ones but still very small, thus requiring some particular care in evaluating the reliability of mineral chemical data. The performed analyses ($n = 466$) were thus selected by discarding data with (CaO + Na₂O + K₂O) >0.5 wt.% and with the sum of oxides <83.0 and >89.5 wt.% [following Vidal and Parra (2000) and Escuder-Viruet et al. (2011)]. In addition, analyses with anomalously high TiO₂ (>0.90 wt.%, where most analyses have <0.30 wt.%) were also cautiously filtered out as likely indicative of mixed rutile-chlorite data points. Considering the above analytical difficulties, we also tested an alternative data filtering strategy and adopted a more conservative confidence interval of 86.0–89.0 wt% for the sum of oxides. Nevertheless, we did not observe any significant difference in the overall chemical features of the analyzed Chl crystals. This can be observed by comparing the Chl plots described below with their alternative versions reported in Figures S2.1 and S2.2 in Supporting Information S1.

Compositions lie between chamosite and clinocllore (Figure S1.1 in Supporting Information S1), with X_{Mg} values [Mg/(Mg + Fe²⁺)] varying mostly from 0.23 to 0.56 (plus one single data point with 0.73), corresponding to ripidolite brunsvigite types (Hey, 1954). The spread in chemical composition reveals Tschermak [^{IV}Al^{VI}AlSi₁(Mg,Fe)₁] and di/trioctahedral substitutions [(Mg,Fe²⁺)₃□₁Al₂, where □ = vacancy; Figures 9a and 9b]. A relatively large compositional range is covered by Si (2.482–3.009 atoms per formula unit, apfu) and R²⁺ cations (3.323–4.622 apfu), while R³⁺ cations and □ are mostly around 3 and <0.5 apfu, respectively (except for a single data point with Si 2.976, R²⁺ 3.323 and □ slightly >0.5 apfu; Figures 9c and 9d). No systematic difference seems evident between Chl crystals from the analyzed metapelite and slate samples, as well as between crystals forming the S₁ and S₂ cleavages in the slate samples (Figures S1.1 and S1.2 in Supporting Information S1).

4.3.2.2. White Mica (Wm)

Wm crystals have remarkably small grain sizes (generally a few μ m in thickness), which made microanalyses extremely challenging. All the acquired data points ($n = 121$) were therefore carefully selected to exclude contaminated intergrown phyllosilicate analyses with (TiO₂ + MnO + Cl) > 0.5 wt.%, as well as unreliable analyses with an oxide sum <92.0 and >97.0 wt.% (Escuder-Viruet et al., 2011; Vidal & Parra, 2000). As in the

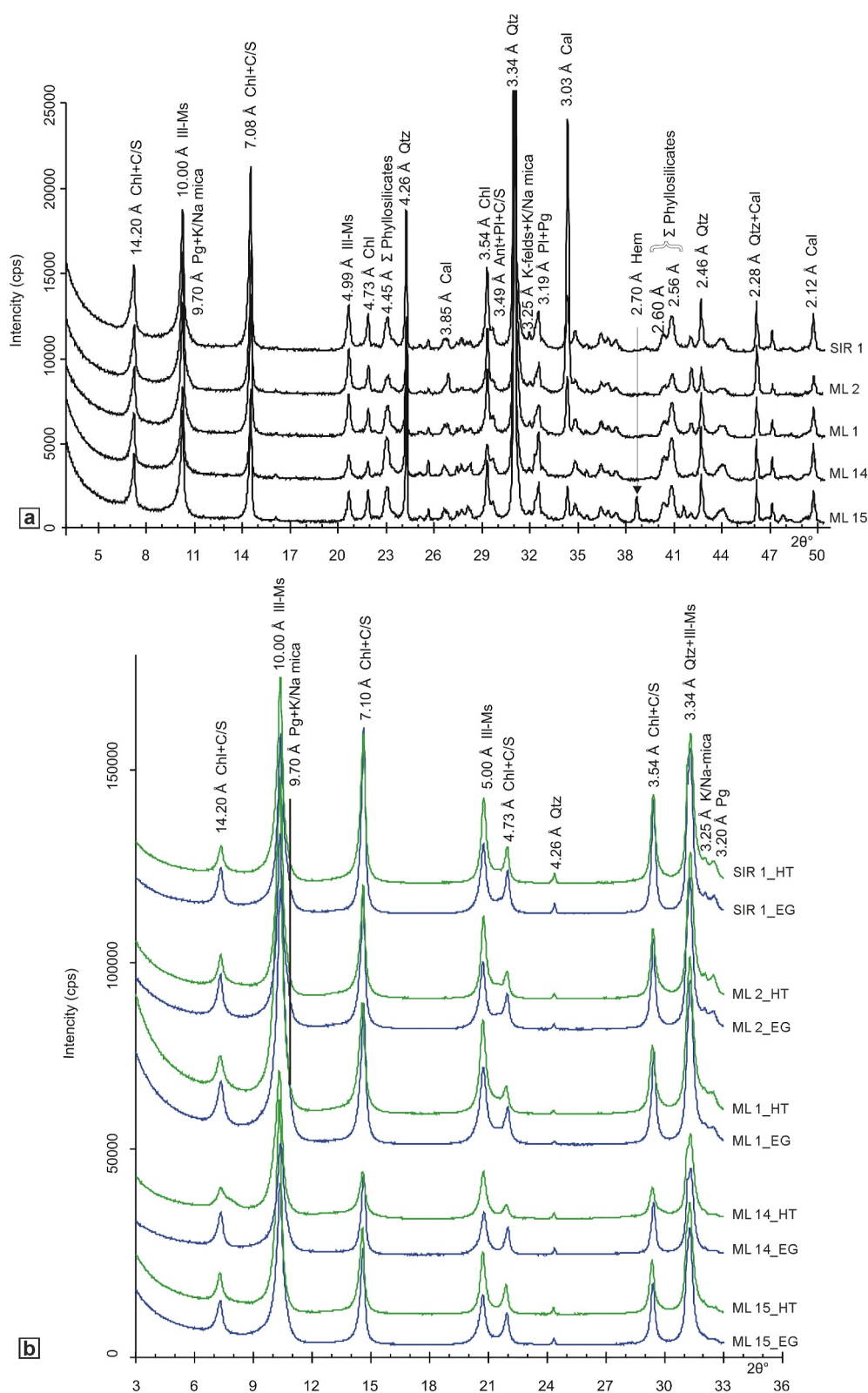


Figure 8. XRD patterns of (a) bulk sample and (b) clay fraction. Chl, chlorite; C/S, mixed layers chlorite/smectite; Ill-Ms, illite-muscovite; Pg, paragonite; K/Na mica, White K-Na mica Qtz, quartz; Cal, calcite; Pl, plagioclases; K-felds, k-feldspars; Ant, anatase; Hem, hematite. EG, glycolated sample; HT, heated sample.

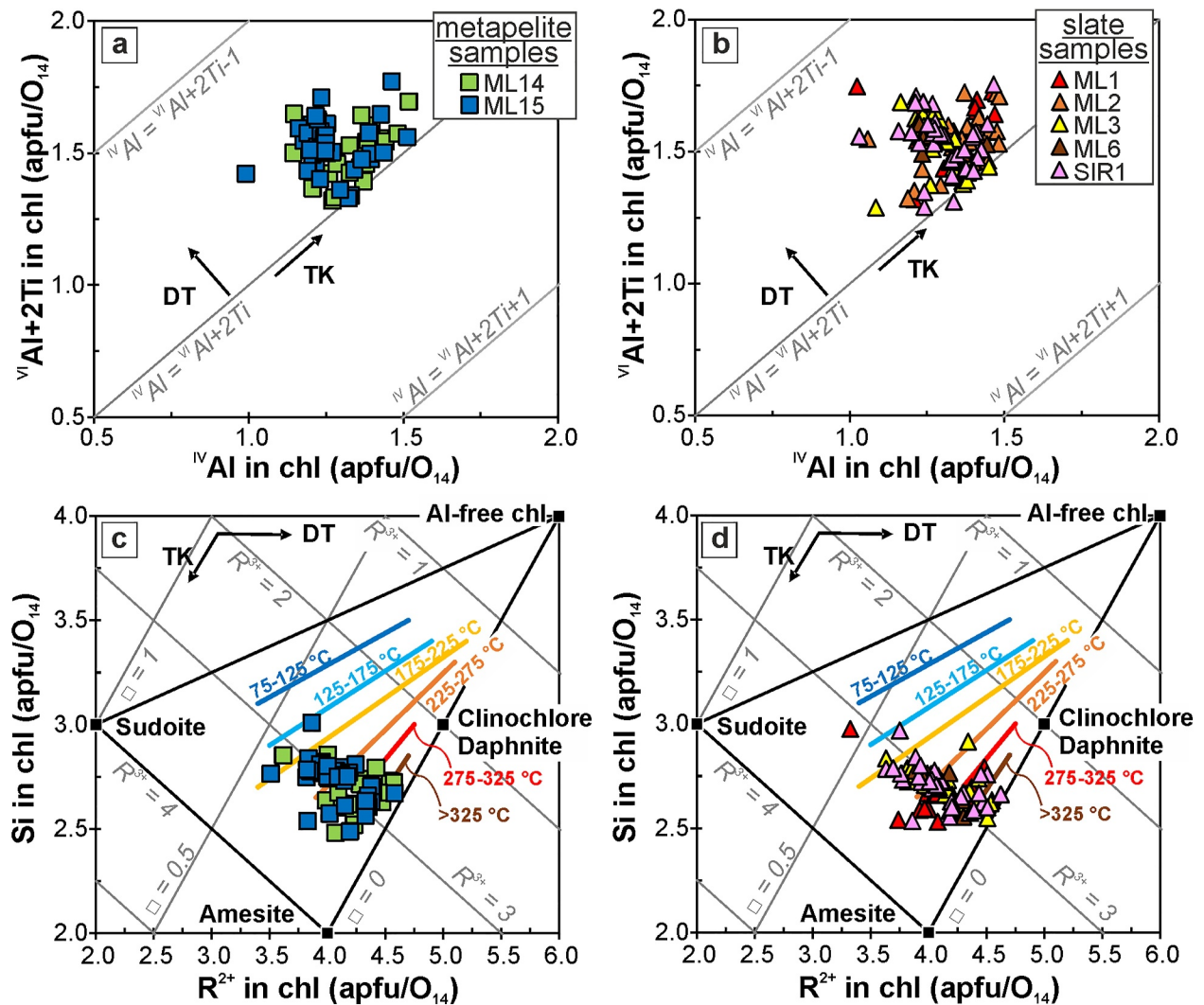


Figure 9. (a, b) $^{VI}Al+2Ti$ versus ^{IV}Al and (c, d) Si versus R^{2+} in chlorite crystals (chl) from the investigated Tempa Roccarossa mélangé metapelite and slate samples. In (c, d), the semiquantitative isotherms after Bourdelle and Cathelineau (2015) are also reported. Arrows point to the effects of the Tschermak (TK) and di/trioctahedral (DT) mineralogical substitutions.

case of Chl, we also tested an alternative data filtering and adopted a more conservative confidence interval of 93.0–97.0 wt.% for the sum of oxides. We again recognized no significant difference in the overall chemical features of the analyzed Wm crystals (see the alternative plots in Figure S2.1 in Supporting Information S1).

The samples investigated show relatively large compositional variation, suggesting some complex mineralogical substitutions. Data points spread along the muscovite-celadonite Tschermak exchange line (Figure 10a) close to the Al_{tot} -rich (2.259–2.867 apfu) and Si-poor (3.021–3.382 apfu) end. Deviations point to an excess of Fe and Mg related to di/trioctahedral substitutions and some ferrimuscovite components (Figure 10b). The pyrophyllitic substitution $[KAlSi_{-1}\square_{-1}]$ is also significant, as indicated by the large range in the total interlayer charge (t.i.c. = $K + Na + 2Ca$; Figure 10c) ranging from 0.714 to 0.956 apfu. The paragonitic substitution (KNa_{-1}) is generally limited, although some Wm crystals with high Na content were also analyzed (>0.200 and up to 0.656 apfu; Figure 10d). The paucity of Wm data for the metapelite samples (only two analyses vs. 51 for the slate samples) does not allow to confidently evaluate any systematic compositional difference between the two rock types.

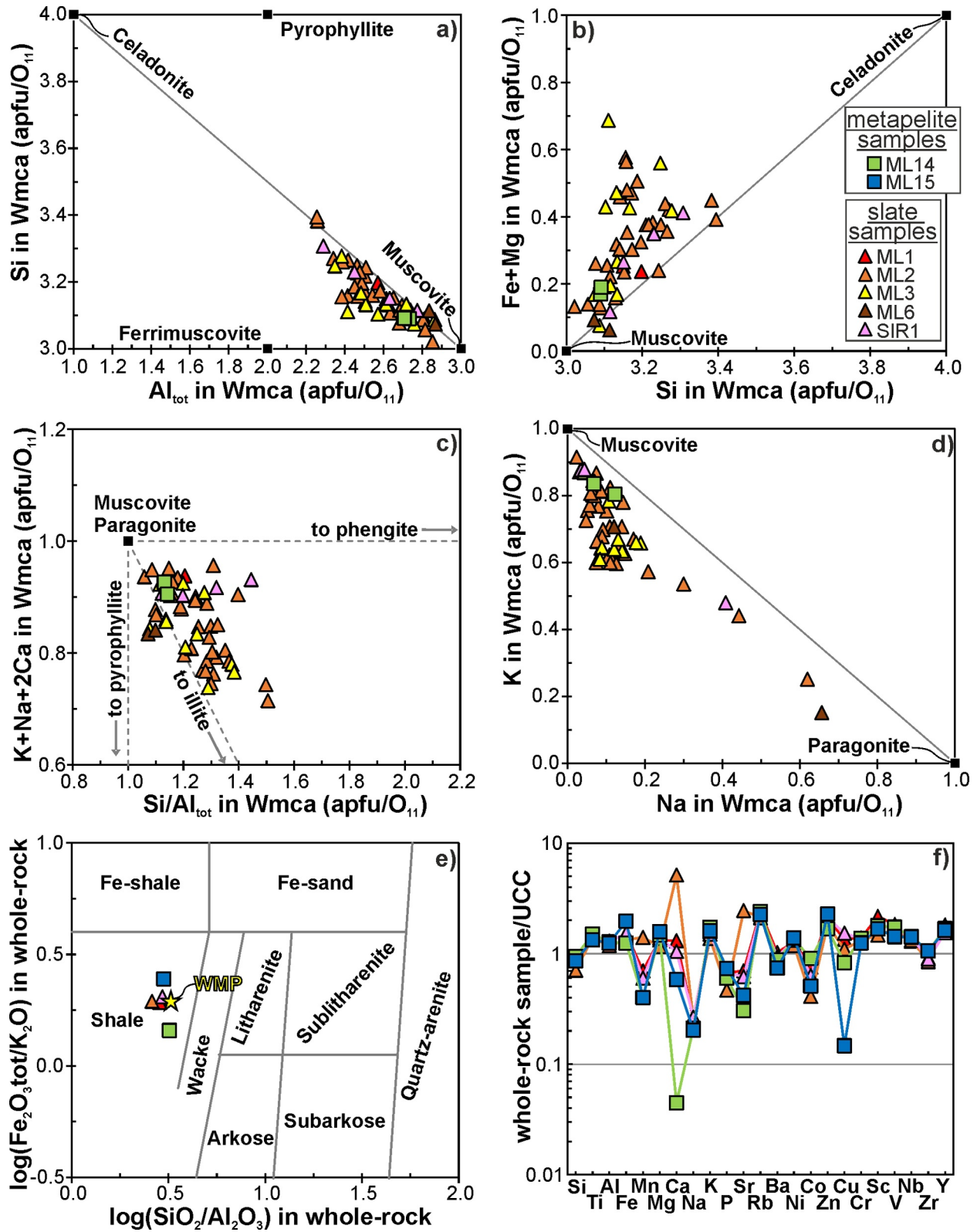


Figure 10. (a) Si versus Al_{tot} , (b) Fe + Mg versus Si, (c) K + Na + 2Ca versus Si/Al_{tot} and (d) K versus Na in white mica (WM) crystals, (e) $\log(Fe_2O_3_{tot}/K_2O)$ versus $\log(SiO_2/Al_2O_3)$ (Herron, 1988) and (f) upper continental crust (UCC; Rudnick & Gao, 2014) normalized major oxides and trace elements in whole-rock for the investigated Tempa Roccarossa mélangé samples.

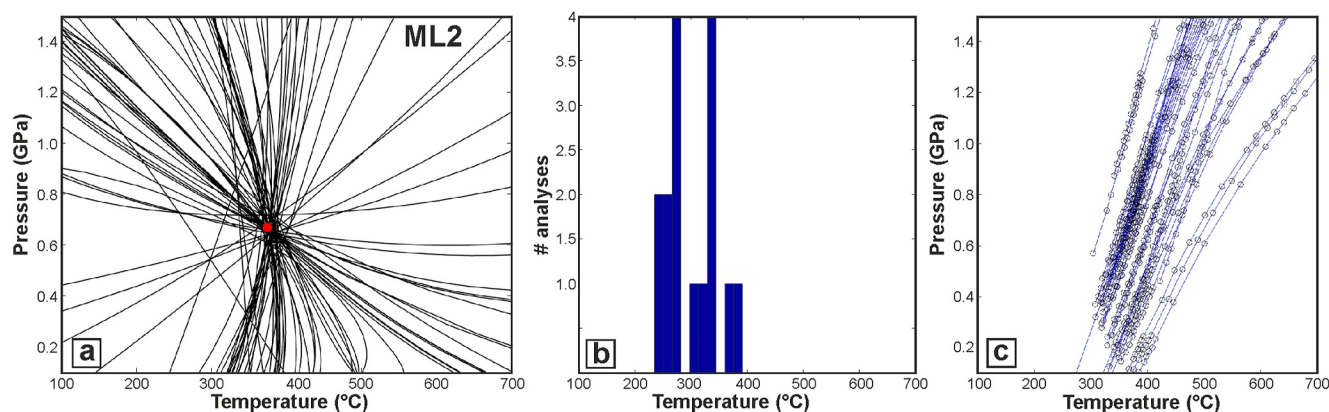


Figure 11. Results of (a) Chlorite + Mica + Quartz + H₂O thermobarometry, (b) Chlorite + Quartz + H₂O thermometry and (c) Mica + Quartz + H₂O thermobarometry for sample ML2. In (c) each line represents an equilibrium between Mica + Quartz + H₂O as a P–T line along which the interlayer H₂O content of the mica varies. A full description of each method can be found in Lanari and Duisterhoeft (2019).

4.3.3. Whole-Rock Composition

The analyzed Tempa Roccarossa mélange samples all fall in the shale compositional field of Figure 10e, showing very homogeneous SiO₂/Al₂O₃, while Fe₂O₃tot/K₂O is more variable, especially for the two metapelite samples. Although generally in agreement with the composition of the Worldwide Median Pelite (WMP) estimated by Forshaw and Pattison (2023), the investigated samples have lower SiO₂ (47.2–58.3 wt.% vs. 63.7 wt.% of WMP; FeO converted to Fe₂O₃tot and sum of oxides normalized to 100 wt.%) and Na₂O (0.66–0.87 vs. 1.37 wt.%), generally higher Fe₂O₃tot (7.47–11.0 vs. 7.55 wt.%), and higher MgO (2.88–3.93 vs. 2.39 wt.%) and CaO (2.08–18.5 vs. 0.65 wt.%), not taking into account sample ML14. The latter is closer to the WMP, that is, 63.0 wt.% SiO₂, 6.96 wt.% Fe₂O₃tot, 0.16 wt.% CaO. Weight loss on ignition (LOI) is generally higher for metapelite (5.83–6.53 wt.%) rather than slate samples (5.21–5.96 wt.%), except for slate sample ML2 which reaches 8.11 wt.%. Compared with the average estimates for upper crustal compositions (UCC; Figure 10f), only a few significant deviations are recognizable, with all samples showing overall comparable patterns. Very slight enrichments are evident for Ti, Al, Fe, Mg, K, Rb, Zn, Cr, Sc, V, Nb and Y, while Na, P, Ba and Co are depleted, well correlating with the generally (potassic) Wm- and Chl-rich and alkali feldspar-poor mineralogy (see previous sections). Slate sample ML2 is strongly enriched in Ca and, less evidently, Sr, and depleted in Si, well in line with the high calcite and low quartz modal abundances revealed by XRPD analyses (Section 4.3.1) and with the higher LOI values. On the other hand, metapelite sample ML15 is enriched in Fe (at almost 2xUCC values) and depleted in Cu (coupled with minor depletions in Ca and Sr), well correlating with the relatively high hematite and low plagioclase and calcite contents. Finally, metapelite sample ML14 is strongly depleted in Ca and Sr, reflecting the absence of calcite, notwithstanding the highest plagioclase modal abundances.

4.3.4. Chl-Wm Multi-Equilibrium Geothermobarometry

We applied the three multi-equilibrium methods to samples ML1–2–6–14 and SIR1. Except for sample ML6, for which Chl and Wm appear to have not recorded chemical equilibrium, there is no convergence of the selected equilibria for the chlorite + mica + quartz + H₂O method in the P–T space; the results indicate temperature and pressure ranges between 300 and 380°C and 0.34 and 0.68 GPa, respectively (Table S2.5 in Supporting Information S1; Figure 11a; Figure S3.1 in Supporting Information S1). Comparable results were obtained by applying the chlorite + quartz + H₂O method for chlorite (Figure 11b; Figure S3.2 in Supporting Information S1) and the mica + quartz + H₂O method for white mica (Figure 11c; Figure S3.3 in Supporting Information S1).

4.4. Strain and Kinematic Vorticity Analyses

To obtain estimations of 3D finite strain, we analyzed only calcareous elliptical markers that were deformed passively, excluding rigid objects. We analyzed pictures of polished slabs and thin sections, obtaining the R_f/ϕ plots of Figures 12a–12e. The 2D finite strain (along R_{XZ} and R_{YZ} planes) varies between 4.50 and 8.26. The ellipsoids fall in the oblate field when plotted in the Ramsay–Flinn diagram (Figure 12f). The latter plot also shows

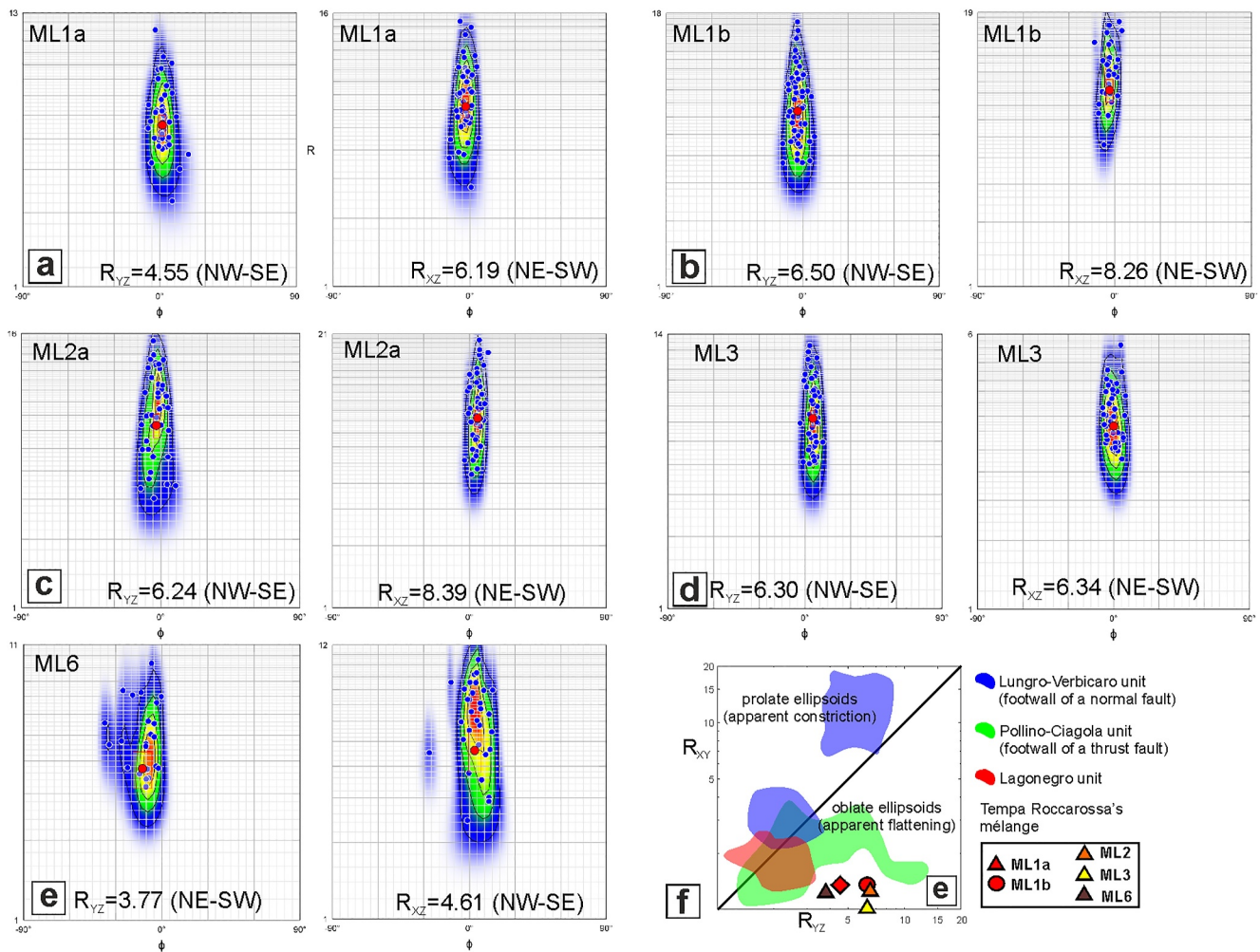


Figure 12. (a–e) R_ϕ/ϕ diagrams and (f) Flinn-Ramsay plot of the investigated Tempa Roccarossa mélangé samples. Data from this work and Mazzoli (1992), Iannace et al. (2007), Vitale and Mazzoli (2009), and Vitale, Prinzi, et al. (2020).

the field of strain ellipsoids estimated in LMB units (Mazzoli, 1992) and mylonites of other southern Apennines units, formed in shear zones at footwall of a major thrust (Pollino-Ciagola unit; Iannace et al., 2007; Vitale & Mazzoli, 2009) and a regional normal detachment (Lungro-Verbicaro unit; Iannace et al., 2007; Vitale, Tramparulo, et al., 2020). It is worth noting that, in the analyzed samples, the maximum stretching (X -axis) always occurs along the direction parallel to the NW-SE tectonic transport.

The kinematic vorticity analysis, performed on the synthetic $S-C'$ structures (R_2), indicates similar results for the four analyzed slate samples (Figures 13a–13d). The mean θ angles range between 19 and 22°, with a Gaussian distribution, indicating mean kinematic vorticity numbers W_k of 0.92–0.94. On the other hand, the method of rigid porphyroclast analysis (Figures 13e–13h) yields mean values ranging from 0.88 to 0.90. These values, reported in the diagram of Figure 13i, provide a percentile of the coaxial strain of 20%–35%, that is, the contribution of the pure shear with respect to the simple shear (e.g., Fossen & Cavalcante, 2017; Means & Park, 1994; Tikoff & Fossen, 1995).

5. Discussion

5.1. Petrography, XRPD, Chl-Wm Multi-Equilibrium and Temperature Estimation

By integrating microstructural, mineralogical, mineral chemical and whole rock geochemical analyses, we have investigated the thermal equilibrium at which the studied mélangé formed. The mélangé is mainly composed of

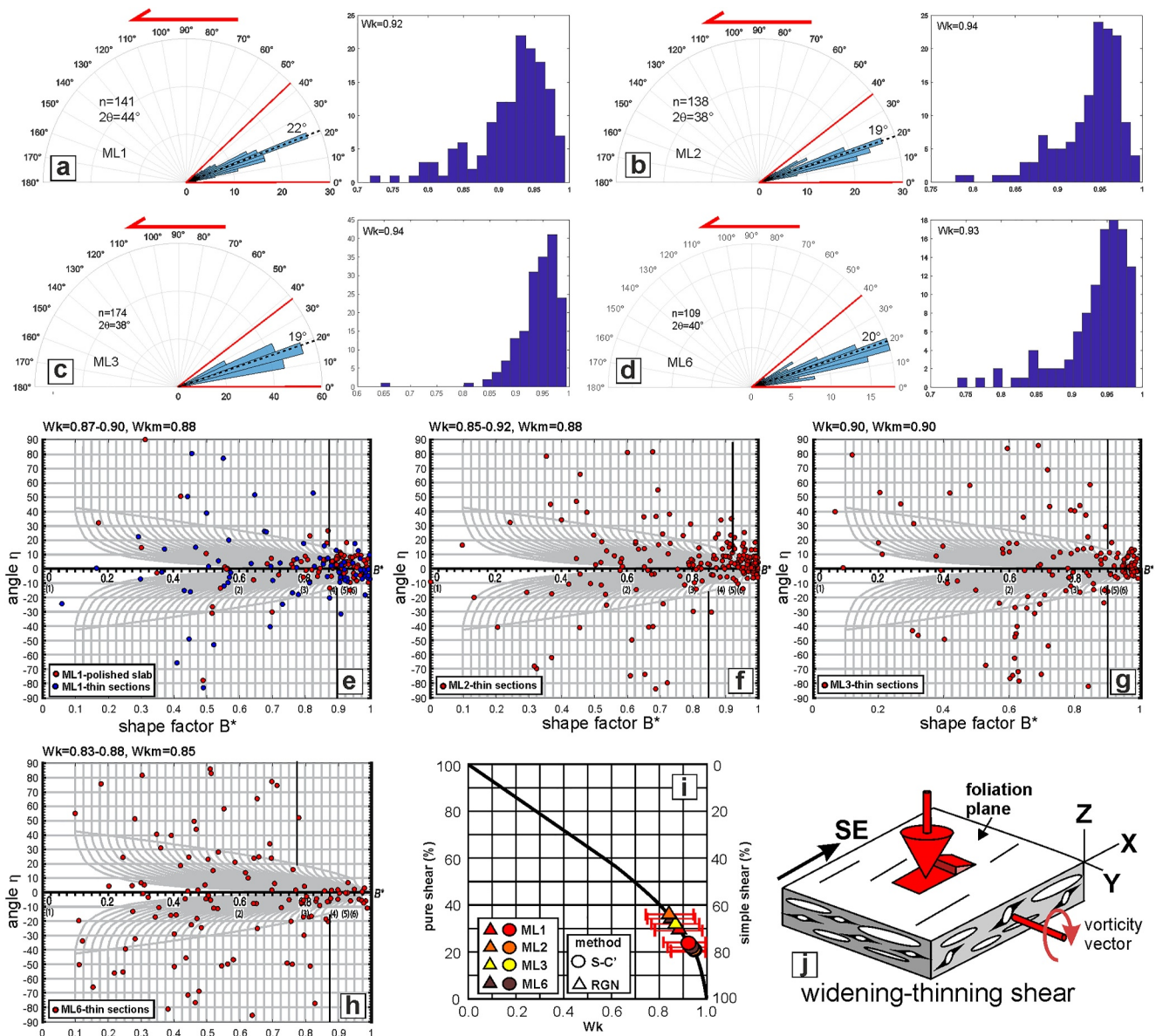


Figure 13. Results of the vorticity analyses performed on the investigated Tempa Roccarossa mélangé samples. (a–d) S-C' structures method: (a) ML1; (b) ML2; (c) ML3; (d) ML6. (e–h) Rigid porphyroclast method: (e) ML1; (f) ML2; (g) ML3; (h) ML6. (i) Wk versus pure shear/simple shear percentile plot (triangle: S-C' structures method; circle: Rigid porphyroclast method). (j) Model of the widening-thinning shear zone (Tikoff & Fossen, 1999).

Wm and Chl minerals, which define the relict (S_1) and main cleavage (S_2). XRPD data show the presence of paragonite and K/Na mica. These minerals occur in the upper part of the late diagenetic zone, and are ubiquitous in the anchizone (Cavalcante et al., 2012; Kisch, 1987; Leoni et al., 1996). The temperature information provided by these phases is somewhat controversial. The KI values obtained from the Wm crystals with size $<2 \mu\text{m}$ indicate that the investigated samples seem to have equilibrated at rather low-T conditions, with metapelite pointing to lower grades ($200 \pm 10^\circ\text{C}$, Table 1) with respect to the slate samples (from 220 ± 10 to $250 \pm 10^\circ\text{C}$). On the other hand, data obtained from empirical geothermometry based on Chl compositions (Figures 9c and 9d), performed by EDS analysis on larger crystals ($5\text{--}10 \mu\text{m}$ thick), not only show a large variability (basically covering the entire spectrum from 125 to $>325^\circ\text{C}$) but also do not recognize any systematic difference between the two rock types and S_1 and S_2 cleavages.

A role in these discrepancies could be related to the well-known intrinsic difficulties of low-T Chl geothermometry in general (and the empirical method used in particular), discussed in detail by Bourdelle and

Table 1
Mineralogical Composition (W %) of Bulk Rock and Clay Fraction

Sample	Bulk sample (wt%)									Clay fraction (<2 μm)				KI and temperatures estimates		
	Ill/Mus	Pg + K/Na mica	Chl + C/S	Qtz	Ant	K-feld	Pl	Cal	Hem	Ill/Mus	Pg	Chl	C/S	FWHM	KI (Basel)	T °C
SIR 1	40.0	3.0	24.0	24.0	<1	1.0	2.0	6.0	0.0	67	9	21	4	0.387	0.310	250 ± 10
ML 2	36.0	3.0	17.0	14.0	1<	1.0	2.0	27.0	0.0	71	10	14	5	0.428	0.343	240 ± 10
ML 1	43.0	6.0	23.0	19.0	1 < 1	1.0	2.0	6.0	0.0	80	6	12	2	0.492	0.394	220 ± 10
ML 14	43.0	tr	23.0	30.0	1 < 1	1.0	3.0	0.0	0.0	81	4	11	4	0.521	0.417	200 ± 10
ML 15	42.0	tr	23.0	25.0	<1	1.0	3.0	3.0	3.0	79	4	14	3	0.457	0.366	230 ± 10

Note. Kubler Index (KI) and temperature estimates are reported. Ill/Mus, illite-muscovite; Pg, Paragonite; K/Na mica, White K-Na mica; Chl, chlorite; C/S, mixed layers chlorite/smectite; Qtz quartz; Ant anatase; k-feld alkali feldspar; Pl plagioclase; Cal calcite; Hem hematite; FWHM Full Width at Half Maximum. The temperature estimates (in bold) for sample ML14 are discussed in the text.

Cathelineau (2015), Bourdelle (2021), and Petroccia et al. (2025). Nevertheless, the large temperature range and the completely overlapping compositions of the crystals aligned along the S_1 and S_2 foliations (Figures S1.1 and S1.2 in Supporting Information S1) could simply indicate the presence of some detrital Chl crystals (e.g., Lanari et al., 2012; Petroccia et al., 2025). This is particularly evident for the crystals with the highest T values, which fall well within the epizone (or chlorite zone/greenschist facies), and which appear to be at odds with the very fine grain size of the studied Tempa Roccarossa mélange samples. The T estimates obtained from the various multi-equilibrium methods applied are significantly higher than those obtained from the KI. However, since these were obtained using SEM-EDS analyses performed on the larger grains, it seems likely to conclude that the first are detrital in origin, while the second include the neo-formed equilibrium crystals, which thus provide the most reliable geothermobarometric estimates.

However, only detrital Wm crystals have been described in the *Monte Facito* Formation (Ciarapica & Passeri, 2000; Passeri & Ciarapica, 2010), while Chl crystals have only been found in the Roccarossa mélange (Mazzoli, 1992). It follows that the abundance of Chl and Wm grains in the mélange suggests that they originated from the tectonic erosion of the Paleozoic rocks during the decollement activity. This is a common feature of mélange rocks, including exotic materials (Festa et al., 2019). In this light, the Chl-Wm crystals could be in thermal equilibrium, recording a previous P-T evolution likely associated with the Variscan orogeny, such as observed in metapelite units in Calabria (e.g., Graessner & Schenk, 1999).

The presence of unequilibrated detrital grains is commonly recognized from the observation of zoning patterns, often with the aid of compositional mapping (e.g., Lanari et al., 2012; Petroccia et al., 2025). However, considering the extremely small grain size of the investigated Chl (as well as Wm) crystals, it is conceivable that the very low-grade conditions reached by the Tempa Roccarossa mélange may have significantly slowed reaction kinetics, possibly allowing P-T re-equilibration only for the finest Wm fraction (size <2 μm).

The trend of increasing KI-estimated T values from the metapelite to the slate samples, which lines up with metapelite samples having lower amounts of paragonite (e.g., Guidotti & Sassi, 1998) and higher LOI values (if the calcite-rich slate sample ML2 is excluded; see Forshaw & Pattison, 2023), could be taken as further evidence for the overall consistency of these T estimates.

In summary, the above observations suggest that T values obtained from Chl geothermometry may be less reliable in the presence of detrital grains than those obtained from KI values. Therefore, the latter will be used in the following discussion to reconstruct the tectono-metamorphic evolution of the Tempa Roccarossa mélange.

5.2. Strain, Structures and Kinematics

Strain and kinematic analyses provide significant information on the orogenic evolution of the LMB units. The analyzed meso- and microstructures suggest that the mélange was formed within a shear zone. Hence, these highly deformed rocks can be described as a sheared mélange (*sensu* Needham, 1995). The FSEs, estimated from slate samples (ML1,2,3,6), all located close to the thrust, fall in the apparent oblate field (Figure 12f). However,

this flattening may be true or related to a volume loss orthogonal to the shear planes. On the other hand, the results of the kinematic vorticity analysis indicate that a pure shear component is present, ranging between 20% and 35% (Figure 13i). Therefore, we can hypothesize a further stretching along the Y -axis, that is, orthogonal to the shear direction (X -axis) suggesting that part of the flattening is related to the pure shear component. Although evidence for microstructures associated with a volume decrease is poorly represented, such as the cleavage S_1 marked in the calcareous porphyroclasts by stylolites at high angles to the bedding, we cannot exclude that a volume loss has occurred. This process could also be associated with the water release due to the chemical reactions transforming (dioctahedral) smectite into illite through mixed illite/smectite layers, and subsequently into muscovite white mica (Cavalcante et al., 2023; Elliott & Matisoff, 1996; Srodon, 1999; van de Kamp, 2008), as well as those transforming (trioctahedral) smectite into chlorite through mixed layers chlorite/smectite (e.g., Beaufort et al., 2015; Robinson et al., 2002). This reaction also produces H_2O , silica and other cations, which result in the final growth stages of quartz crystals in the syntaxial veins (Figures 6c and 7j).

The oblate finite strain of the Tempa Roccarossa mélange is similar to the FSEs calculated for other Apennine units (Figure 12f). Compared to the ellipsoids reconstructed in Mazzoli (1992) for the LMB units, including the Roccarossa locality (red area in Figure 12f), our data indicate a more intense deformation toward the oblate field.

Several structures, such as sigma porphyroclasts, synthetic and antithetic $S-C'$ structures (R_2 and R_1 , respectively), $S-C$ structures, late cleavage (S_3) and the crenulation lineation L_3 mark well the NW-SE shear direction, that is, the X -axis of the FSE. However, the pure shear component was likely characterized by a secondary stretching orthogonal to the shear direction. Accordingly, the ductile shear zone experienced thinning-widening shear, as illustrated in Figure 13j (Tikoff & Fossen, 1999). As a result of the flattening, the mélange rocks are S -tectonites dominated by foliation with no well-marked stretching lineation. The tectonic transport to the E/SE is consistent with the first deformation stage affecting the LMB units as described by Catalano et al. (2007), and the early fold and thrust verging to the E/SE hosted by Mt. Sirino (Mazzoli, 1992). This orientation is also more generally consistent with the orogenic vergence of the southern Apennines, which ranges from NE to SE (e.g., Ciarcia & Vitale, 2025).

Regarding the kinematic vorticity number estimates, the different W_k values obtained by the two methods, that is, rigid porphyroclasts ($W_k = 0.85$ – 0.90) and the synthetic $S-C'$ structures (0.92 – 0.94), could be explained considering that the R_2 shear planes frequently bound the porphyroclasts (Figure 5m), reducing the rotation angle, and thus overestimating the pure shear component. However, considering an uncertainty of ± 0.1 (Iacopini et al., 2011; Tikoff & Fossen, 1995), a common interval of 0.85 – 0.95 is obtained, indicating a percentage of 20%–35% for the pure shear contribution. In any case, the use of different approaches to estimate the kinematic vorticity can reduce the uncertainty of this important tool to evaluate the contribution of coaxial and non-coaxial strain in shear zones (e.g., Xypolias, 2010).

Structural analyses of meso- and micro-structures indicate that the Tempa Roccarossa mélange is characterized by three cleavages (S_1 – S_2 – S_3), with the remnants of the original bedding (S_0) occurring only in the large calcareous porphyroclasts (Figures 4b–4g). S_1 appears as a disjunctive cleavage preserved in some large porphyroclasts (Figures 4c and 4e) or in the microlithons of the subsequent crenulation cleavage S_2 (Figures 5b and 7b–7f). Both S_1 and S_2 are defined by chlorite and white mica (Figures 7b–7f), with chlorite crystals showing no systematic compositional differences associated with each deformation phase (Figures S1.1 and S1.2 in Supporting Information S1). However, the presence of cataclastic relicts around the large porphyroclasts, preserved in the strain shadows (Figure 6h), suggests that the base of the *Monte Facito* Formation was affected by cataclasis prior to ductile strain. In such a tectonic framework, it is hypothesized that part of the chaotic texture results from an early brittle deformation (D_0 stage), which was subsequently enhanced by ductile strain (D_1 – D_2 – D_3 stages). Under this light, the cataclastic rocks associated with the décollement of the LMB units from the autochthonous Paleozoic basement may have acted as a brittle precursor of ductile strain localization, such as observed in other orogenic chains (e.g., Mancktelow & Pennacchioni, 2005; Pennacchioni & Mancktelow, 2007). Further, the cataclastic fabric with displaced clasts of older cataclasis suggests that multiple cataclastic events affected the mélange during its early formation.

Further information on the deformation history is provided by the syn-kinematic veins located within the strain shadows of the porphyroclasts (Figures 6b–6g). These veins exhibit symmetric antitaxial growth of fibrous calcite (e.g., Bons & Montenari, 2005), characterized by sigmoidal or complex shapes, as indicated by the medial line located in the middle of the veins (Figures 6d and 6f). These geometries can result from the rotation of the strain

field or, more likely, from the rotation of the veins (Bons & Montenari, 2005). In this case, vein rotation was a consequence of the porphyroclast rotation during shearing. As typical for brittle-ductile contexts (e.g., Cardello et al., 2024), the veins continued to grow until this syn-kinematic growth ended before the D_2 event, as indicated by the deformed veins transposed by the S_2 cleavage (Figure 6e). The main S_2 foliation is locally deformed by a crenulation with formation of a S_3 cleavage and is widely deformed by antithetic and synthetic S-C' structures. S_3 cleavage and S-C' structures are likely formed in the same deformation stage (D_3).

In summary, the tectonic *mélange* was initially characterized by brittle deformation (D_0) and subsequently by a dominant ductile general strain, defined by the interplay between simple shear, pure shear, and volume change, which occurred in three main stages (D_1 - D_2 - D_3).

5.3. Burial and Exhumation Evolution

In this section, we compare our results with those of previous works to shed light on the dynamic evolution of the burial and exhumation of the LMB units during the Cenozoic orogenic construction of the southern Apennines. Unlike Catalano et al. (2007), who associate the *mélange* formation with the overthrusting of the ApeP onto the LMB, more up-to-date regional geology evidence suggests that the analyzed *mélange* formed in the hanging wall of the major décollement. This allowed the detachment of the LMB units from the Palaeozoic succession during the Tortonian-Pliocene orogenic shortening and the following stacking and overthrusting onto the ApuP (Mazzoli, Barkham, et al., 2001; Mazzoli, Zampetti, & Zuppetta, 2001). This evidence is also supported by the presence of lithoclasts of Fusulinidae-bearing Permian sandstones included in the *mélange* in the Serra Maula (Mt. Facito area; Figure 1a; Ciarapica & Passeri, 2000) and by Chl and Wm in the analyzed Roccarossa *mélange*. In this sense, the latter, located at the base of the Monte Facito Formation, was progressively formed at the base of the LMB units. It is exposed in several places in the central sector of the chain (e.g., in the Mt. Facito area to the north and in the Mt. Sirino and Mt. Alpi areas to the south), and it has been intercepted in several boreholes (ViDEPI Project, 2025), the correlation of which indicates that it was formed by a far traveling overthrust along tens of kilometers. The resulting present-day configuration within the LMB units features the *mélange* embedded within the LMB stacked thrust sheets and positioned on top of the ApuP. This scenario is evident at Mt. Alpi, the only place in the southern Apennines where the otherwise buried ApuP succession is exposed, as reported by Corrado et al. (2002), Mazzoli et al. (2006), La Bruna et al. (2018), and Cavalcante et al. (2023). The authors highlighted the high strain recorded by the ApuP units, as well as by the upper Messinian clastic deposits located below the tectonic *mélange*. Corrado et al. (2002) analyzed the vitrinite reflectance and clay mineralogy of the upper Messinian clastic units, indicating rapid burial to a depth of approximately 4 km in the Early Pliocene due to the overthrusting of the allochthonous wedge. Mazzoli et al. (2006) proposed a temperature range of 110–170°C, based on vitrinite reflectance and I/S mixed layers in clayey sediments, and a temperature of 90–170°C, based on fluid inclusions within calcite veins hosted in the Messinian sandstones. The Authors related these temperatures to the maximum burial associated with the overthrusting of the LMB units onto the ApuP (Table S3 in Supporting Information S1). This aligns with the work of Mazzoli et al. (2008), who provided a synthesis of the thermal indicators in the southern Apennines, suggesting that parts of the allochthonous units have been buried to depths >5 km. More recently, Cavalcante et al. (2023) analyzed the clay mineral composition of ApuP, the *mélange*, and the overlying LMB thrust sheet in Mt. Alpi. The results indicated temperatures of 120–130°C for the upper Messinian units, corresponding to burial depths of 6–7 km, assuming a geothermal gradient of 20°C/km (Sciannina et al., 2004; Megna et al., 2014). The Authors also noted that the *mélange* and the overlying LMB unit exhibit slightly higher thermal equilibrium, with temperatures of 130–140°C. Table S3 in Supporting Information S1 shows the percentage of illite in the mixed illite/smectite layer determined by different studies (Aldega et al., 2003; Cavalcante et al., 2023; Mazzoli et al., 2006, 2008) in the Mt. Alpi area, and temperature estimates determined following Waliczek et al. (2021).

Despite these regional constraints, few studies have focused on the Tempa Roccarossa succession. Aldega et al. (2003) investigated fluid inclusions in calcite veins hosted in the *Monte Facito* Formation, yielding a temperature range of 130–180°C. Catalano et al. (2007) determined paleotemperatures using the Kubler Index in samples from the *Monte Facito* Formation, collected at various locations, including the Tempa Roccarossa locality. This analysis suggests a maximum temperature range of 220–250°C, in good agreement with our estimates, and a maximum burial depth of 8–9 km. Additionally, other rocks of the LMB have been analyzed with the Kubler Index, such as the Jurassic argillites of Mt. Sirino (Mazzoli, Zampetti, & Zuppetta, 2001), which yield deep

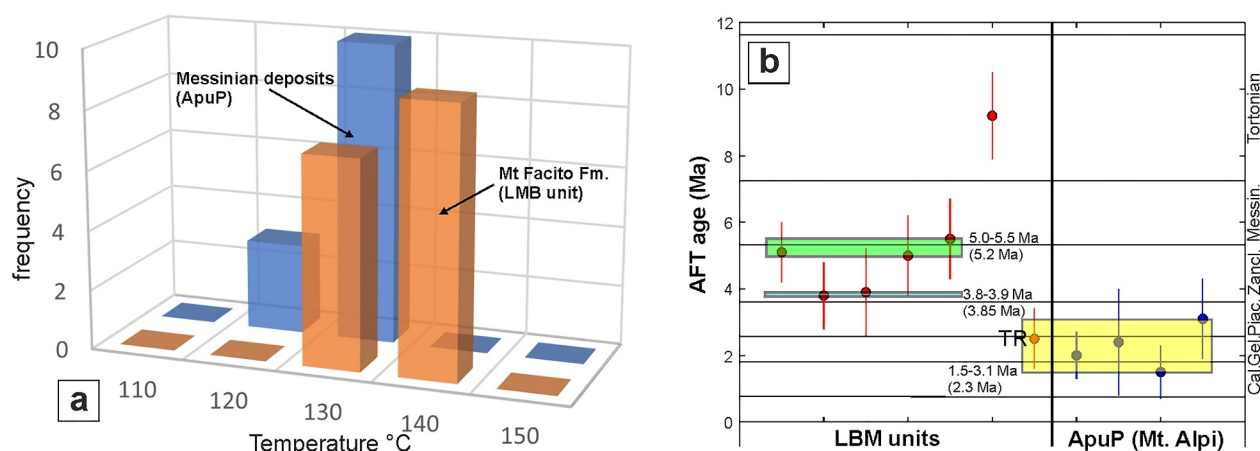


Figure 14. (a) Frequency histograms of temperatures calculated by Illite/smectite ratio for the *Monte Facito* Formation (LMB) and upper Messinian formation of the Apulian Platform (ApuP; Mt. Alpi). Data from Aldega et al. (2003), Mazzoli et al. (2008), and Cavalcante et al. (2023) (Table S3 in Supporting Information S1). (c) Comparison between Apatite Fission Track (AFT) ages of LBM units and ApuP (Mt. Alpi). Data from Mazzoli et al. (2008).

diagenetic zone conditions, or the successions in Sasso di Castalda and Pignola-Abriola (Figure 1a; Schiattarella et al., 2006), which also point to the uppermost diagenetic zone.

Our findings further confirm the evidence of low-grade metamorphism recorded by the *mélange* at the base of the LMB unit. Considering that the current geothermal gradient increases from the front of the chain (17–20°C/km) to the inner sectors (20–26°C/km) of the southern Apennines (Sciamanna et al., 2004; Megna et al., 2014; log of Roccarossa01, ViDEPI Project, 2025), a gradient of about 20°C/km can be proposed for the early stages of the accretionary wedge growth. Then, the maximum paleotemperatures of $250 \pm 10^\circ\text{C}$ obtained for the slates in Site 1 correspond to a tectonic load between 12 and 13 km (about 0.32–0.35 GPa considering a geobaric gradient of 0.027 GPa/km).

However, in analogy to other shear zones associated with large thrusts (Cardello et al., 2024; Graham & England, 1976; Maino et al., 2020; Mori et al., 2015), the effects of thermal shearing need to be considered when interpreting the thermal evolution and deformation mechanisms of a *mélange*. This is crucial as shear heating can significantly increase local temperatures by at least 50–60°C (Cardello et al., 2024; Graham & England, 1976; Maino et al., 2020; Mori et al., 2015; Petroccia et al., 2022), thereby affecting recrystallization in shear zones. Therefore, temperatures obtained from mineralogical analyses in high-strain zones may be higher than those predicted solely by the burial depth of the host rock. The effects of shear heating may explain the difference in temperatures estimated for the more deformed slate samples, located close to the thrust fault (Site 1; $T = 250 \pm 10^\circ\text{C}$), and those for the less deformed metapelites, situated further away (Site 2; $T = 200 \pm 10^\circ\text{C}$). In this case, the thermal gradient is 50°C for a *mélange* thickness of about 25 m, resulting in a value of 2°C/m.

What is also worth noting is that T estimates obtained from the multi-equilibrium methods do not show any correlation with sample location with respect to the thrust fault. This suggests that the larger (detrital) crystals did not re-equilibrate under the new P-T conditions, notwithstanding the additional heat pulse provided by the shear heating.

Thus, to reconstruct the burial history of the *mélange*, we collected all available geothermal estimates published from the LMB and ApuP successions. The frequency plot of temperatures calculated for the *Monte Facito* Formation (LMB) and the upper Messinian units (ApuP) (Figure 14a) shows that the *Monte Facito* Formation reached higher values than the overthrust upper Messinian rocks. This is consistent with the vitrinite reflectance values calculated for the LMB units, which are higher than those values measured in the underlying ApuP succession (Aldega et al., 2003; Mazzoli et al., 2008; Sciamanna et al., 2004). This implies that the LMB units recorded an earlier phase of burial and heating before piling up and thrusting over the ApuP (Mazzoli et al., 2006, 2008; Sciamanna et al., 2004). Furthermore, Mazzoli et al. (2008) highlighted that ApeP units of the Apennine platform, overlying the LMB units, show a lower thermal equilibrium and suggested that the present thickness of the ApeP (generally less than 1 km, as resulting from geological cross sections; Mazzoli et al., 2008) cannot

account for the burial and thermal conditions recorded by the LMB units in the intermediate footwall. Hence, there are paleo-thermal breaks between the LMB units and the overlying ApeP and underlying ApuP rocks. This difference is further amplified by the low-grade metamorphism recorded by the tectonic mélange, as evidenced by the clay mineralogy of the Tempa Roccarossa mélange.

Information about the exhumation of the LMB units and Mt. Alpi was obtained by apatite fission track analysis (AFT; Figure 14b) by Mazzoli et al. (2008). The Authors suggested that the Tempa Roccarossa rocks recorded a cooling age (above the 110–70°C temperature interval) of about 2.3 Ma, similar to Mt. Alpi. The other AFT ages obtained for the LMB units indicate a cooling age of 9.2 ± 1.0 Ma for the Miocene sedimentary units and two clusters around 5.2 and 3.85 Ma for the Mesozoic rocks. We suggest that the Miocene LMB rocks were off-scraped and detached from the older rocks, and then frontally accreted (e.g., Mattioni et al., 2006), resulting in an older exhumation history. On the contrary, the Mesozoic LMB succession, overthrust by the ApeP units, was buried and exhumed in more recent times.

According to Mazzoli et al. (2006) and Schiattarella et al. (2006, 2017), to explain the thermal breaks between the different thrust sheets of the southern Apennines, tectonic delamination by low-angle normal faults (LANFs) should be assumed, which significantly reduced the thickness of allochthonous wedge during the Tortonian-Pliocene time. LANFs are widely reported in the southern Apennines (Casciello et al., 2006; Ferranti & Oldow, 1999; Novellino et al., 2025; Vitale, Prinzi, et al., 2020), including the Cogliandrino fault (Mazzoli et al., 2006) in the area between Mt. Sirino and Mt. Alpi, which puts the LAC units in contact above the LMB thrust sheets. This results in the tectonic elision of the ApeP. According to Mazzoli et al. (2006), the development of LANFs in this region, and in general in the entire southern Apennines (Ciarcia & Vitale, 2025; Vitale, Prinzi, et al., 2020) was associated with the deep-seated thrusting within the ApuP that triggered the tectonic denudation in the Early Pliocene.

5.4. Tortonian-Quaternary Evolution of the Tempa Roccarossa Mélange and Mt. Alpi

Finally, we summarize all the above-mentioned observations in the cartoon in Figure 15, which illustrates the proposed Tortonian-Quaternary evolution of the Tempa Roccarossa mélange and Mt. Alpi within the framework of the orogenic development of the southern Apennines.

To estimate depth values from thermal data, we assumed an average geothermal gradient of 20°C/km and an average thickness of the original LMB unit of about 3 km (Figure 2e).

The first tectonic stage occurred in the Tortonian—early Messinian interval, when the ApeP units thrust over the LMB units (T_0 , Figure 15a), the latter detached from the Paleozoic basement (T_1 ; Figure 15a). The concurrent brittle deformation and increasing burial allowed the LMB units to transition from brittle (D_0) to ductile deformation (D_1 - D_2 - D_3). In this scenario, the orogenic evolution can be explained by the simultaneous activity of thrusting stages T_0 and T_1 , with regional subsidence and thrusting (T_0) increasing burial and the décollement (T_1), allowing the LMB units to detach from the Paleozoic basement.

After reaching the maximum burial depth, the tectonic exhumation began with the piling up of LMB and the thrusting (T_2) of the whole allochthonous wedge onto the ApuP succession. The latter was buried up to 7 km (Figure 15b) according to the geothermometric estimates (120–130°C; Mazzoli et al., 2006; Cavalcante et al., 2023). In our scheme, the Tempa Roccarossa mélange was buried more than the Mt. Alpi mélange, with a maximum difference of 75°C (considering shear heating of 50°C), corresponding to a burial difference of about 3 km.

As discussed earlier, the comparison of burial temperature estimates obtained for the *Monte Facito* Formation of the LMB with those for the upper Messinian sedimentary units of the ApuP (Figure 14a) suggests that the LMB units were more deeply buried than the ApuP prior to thrusting. The tectonic exhumation of the allochthonous wedge is recorded by the AFT cluster ages of 5–5.5 Ma of the LMB units (Figure 14b), corresponding to the overthrust onto the ApuP.

We suggest that exhumation and unloading were enhanced by tectonic delamination in the hanging wall by LANFs during the latest Messinian-Early Pliocene stage of the orogenic evolution, which may correspond to the enhancement of erosion in the Mediterranean catchments related to the salinity crisis (e.g., Garcia-Castellanos & Villaseñor, 2011). Finally, in the Plio-Quaternary (Figure 15c), the allochthon wedge was further exhumed by the

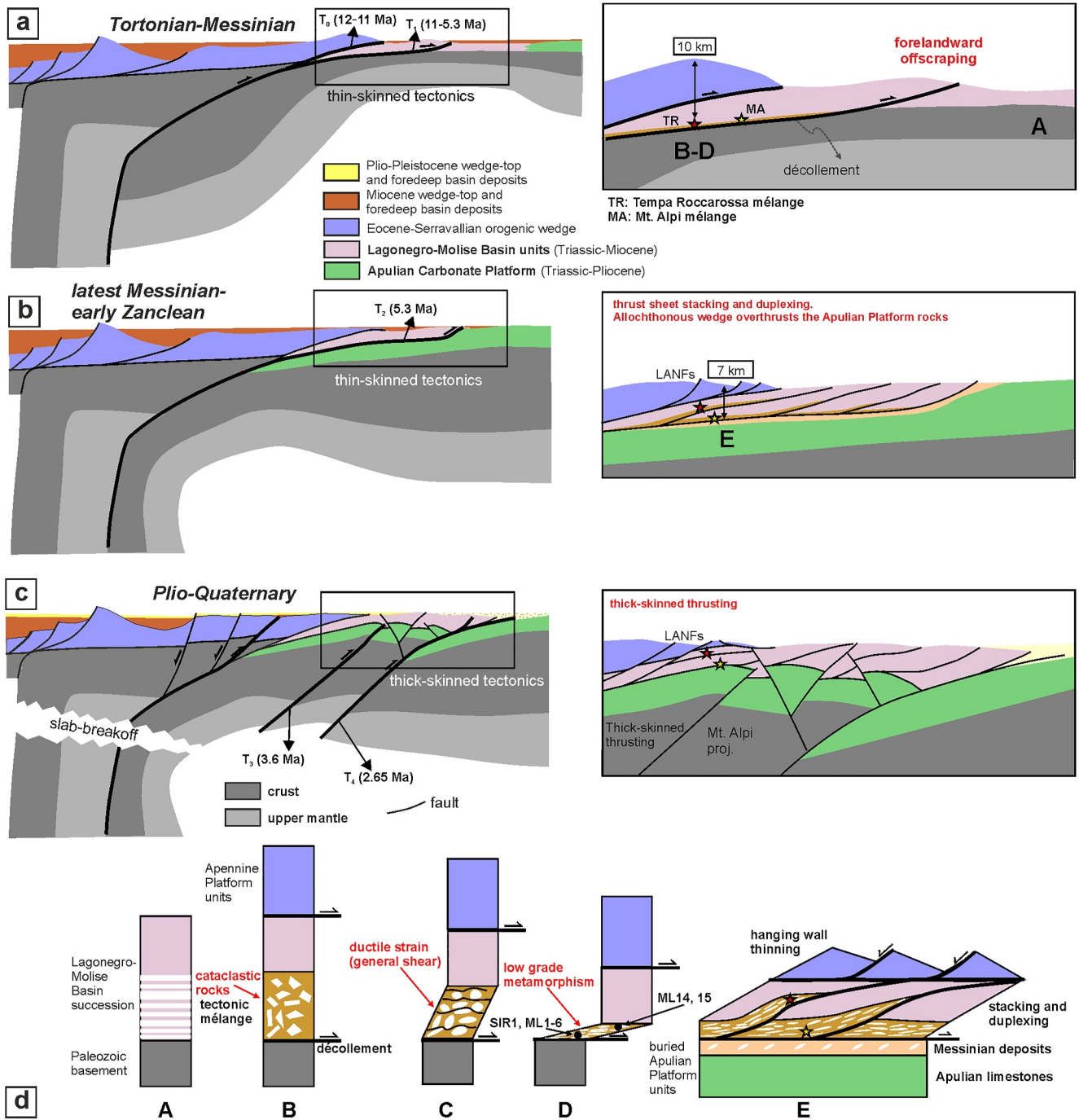


Figure 15. (a–c) Schematic crustal section showing the proposed tectonic evolution from Tortonian to Quaternary for the southern Apennines-Calabria-Peloritani System (modified after Vitale, Ciarcia, et al., 2019; Vitale, Prinzi, et al., 2019; not to vertical scale). (d) Cartoon showing the tectonic and strain evolution of the tectonic mélangé units (modified after Kimura et al., 2012). LANFs: low-angle normal faults.

activity of two main thrusts (T_3 and T_4), which were likely active in the 3.9–3.8 Ma and 3.1–1.5 Ma time intervals, respectively, as indicated by the AFT clustered ages (Figure 14b). In this case, the unloading was due to the activity of LANFs (e.g., Mazzoli et al., 2006), likely associated with out-of-sequence thrusts rooted in the buried Apulian succession (e.g., Ciarcia & Vitale, 2025; Vitale, Prinzi, et al., 2020).

Figure 15d outlines the strain and tectonic evolution of the Roccarossa mélangé. Stage A represents the original succession of the LMB attached to the Variscan basement. Stage B represents the formation of cataclastic rocks

associated with the décollement activity between the LMB and the Variscan basement. The brittle deformation likely formed a clayey matrix-supported cataclasite. Subsequently, this texture was affected by ductile strain and low-grade metamorphism (Stages C-D), reaching temperatures of about $250 \pm 10^\circ\text{C}$ for the highly deformed slates near the principal slip surface of the thrust, which may be partly (50°C) related to the effects of shear heating. Finally (Stage F), LMB thrust sheets piled up by stacking and duplexing, overthrusting onto the ApuP. Meanwhile, LANFs affect the ApeP units, located at the hanging wall of the LMB units, decreasing the thickness and the lithostatic load.

To better explain the thermobaric evolution of the Tempa Roccarossa mélange and the upper Messinian deposits (ApuP) in Mt. Alpi, we reconstructed their P-T-t paths (Figure 16), incorporating all available information, including the results of our study. The base of the *Monte Facito* Formation in the Tempa Roccarossa area was overthrust (T_0) by allochthonous units in the early Tortonian, reaching about $250 \pm 10^\circ\text{C}$. These thermal values correspond to a maximum depth of 12–13 km; however, considering the possible contribution of the shear heating of about 50°C (Cardello et al., 2024; Maino et al., 2020), a depth of 10 ± 0.5 km can be proposed. Synchronously, the succession was detached from the Paleozoic units and subsequently piled up and exhumed onto other LMB units (T_1).

To better constrain the orogenic pulses, we have added some bars to the scheme of Figure 16, indicating the ages of the foredeep deposits for the different tectonic units (e.g., Vitale & Ciarcia, 2018), including the *Serra Palazzo* Formation (Frigento Unit, LMB), the *San Giorgio* Formation (Sannio Unit, LMB), the *Torrente Flaga* Formation (Fortore Unit, LMB), the inner and outer buried ApuP, and finally, the Bradanic foredeep sediments (ApuP).

In the early Zanclean (earliest Pliocene), the allochthon was thrust over the ApuP (T_2), burying the Mt. Alpi succession (MA) to a depth of about 5–7 km (120 – 130°C ; Cavalcante et al., 2023; Mazzoli et al., 2006). It should be emphasized that the vertical distance between the Tempa Roccarossa mélange and the ApuP in the *Tempa Roccarossa* well (Figure 2e) is currently about 3 km. However, the orogenic position of Tempa Roccarossa is more internal than that of Mt. Alpi, making it reasonable to assume that the ApuP below the mélange was deeper buried than Mt. Alpi.

Finally, both the Tempa Roccarossa and Mt. Alpi successions were exhumed during the T_3 and T_4 thrusting events, which crossed the 110 – 70°C AFT isotherm in the 3.1–1.5 Ma time interval (Figure 14b). Regarding the three ductile deformation phases recorded by the tectonic mélange that allowed the formation of the three cleavages (e.g., Figure 7f), we suggest that the D_1 – D_2 stages occurred under low-grade metamorphism at 10 km depth. In contrast, the D_3 deformation occurred during the subsequent thrusting and exhumation.

6. Conclusions

The present study contributes to the understanding of tectonic mélanges, providing an example from the southern Apennines. This work examines the Late Miocene–Early Pleistocene orogenic dynamics of the area in terms of the relationships between tectonics and burial and exhumation history. We examined the tectonic mélange that initiated this deformation by detaching the Meso-Cenozoic pelagic succession from the autochthonous Paleozoic basement. Meso- and microstructural analysis, combined with strain and kinematic investigations, and the results of petrographic, mineralogical, mineral-chemical, and whole-rock geochemical analyses, allowed us to reconstruct the P-T-t path for these rock units.

The main result of our study is the recognition of a ductile deformation consistent with the estimated temperature peak of $250 \pm 10^\circ\text{C}$ obtained from the Kubler Index on the fines fraction (size < 2 mm) of Wm. However, considering a 50°C contribution from shear heating, the burial depth is estimated to be 10 km (about 0.3 GPa), assuming an average paleogeothermal gradient of $20^\circ\text{C}/\text{km}$. Furthermore, the thermobaric evolution of the Tempa Roccarossa mélange and the upper Messinian ApuP units in Mt. Alpi was reconstructed. The analyzed mélange is located at the base of the LMB unit, overriding another LMB thrust sheet. A similar mélange is exposed near Mt. Alpi, at the top of the ApuP succession, below the LMB unit, and characterized by lower thermal equilibrium. Both mélange units began to form at the same décollement level at the base of the *Monte Facito* Formation. However, the structural position of the Tempa Roccarossa mélange, along with its higher thermal equilibrium, suggests that it was in a more internal position and subjected to a higher lithostatic load compared to the Mt. Alpi mélange. Further, a thermal break is also identified between the LMB units and the Apulian succession of Mt. Alpi, suggesting that the LMB units were buried to greater depths prior to orogenic coupling with the Apulian

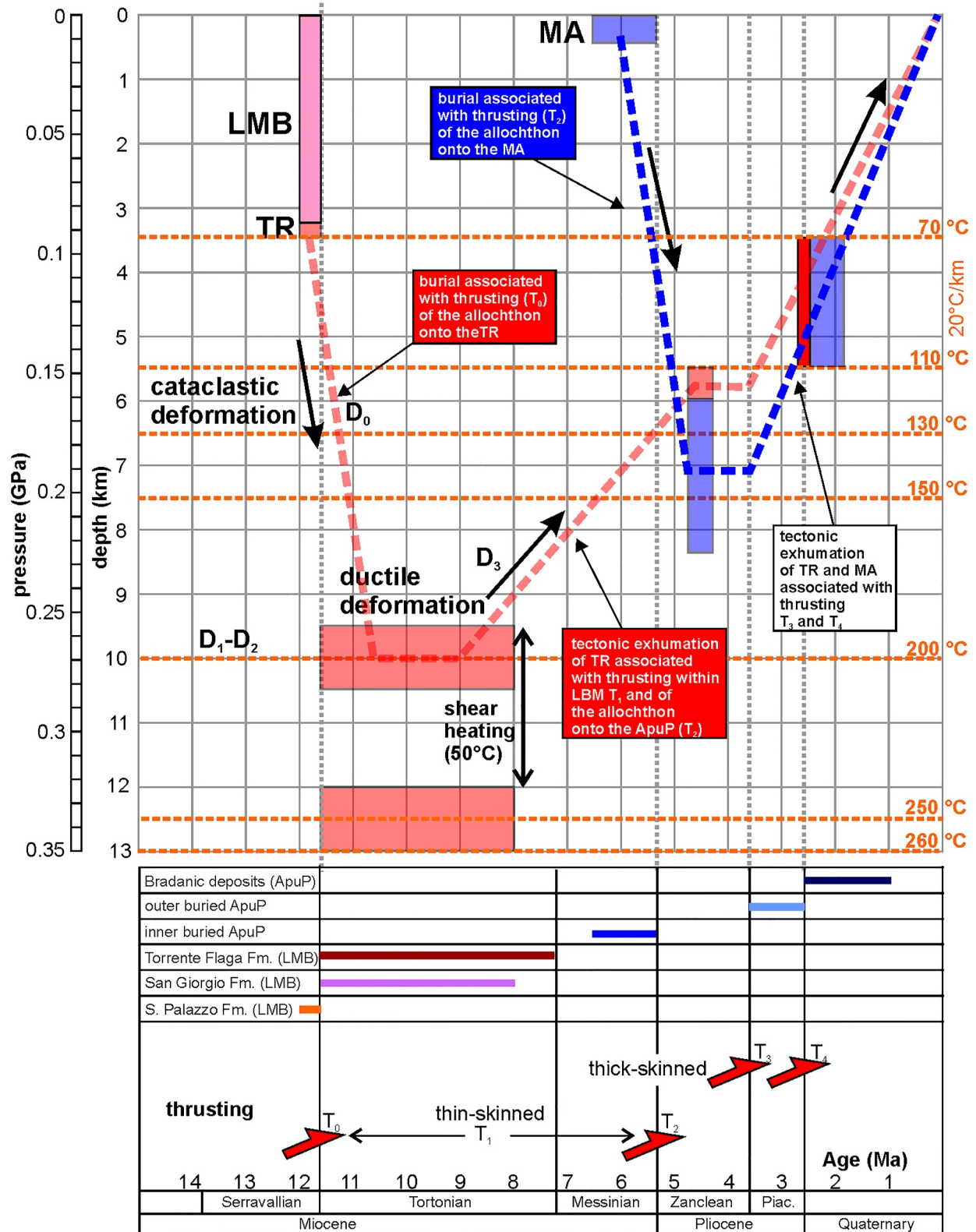


Figure 16. Reconstructed P-T-t paths for the Tempa Roccarossa (TR) mélangé and Mt. Alpi upper Messinian units (MA).

succession. This evidence suggests that the LMB units were exhumed and unloaded before being thrust over the ApuP succession. The unloading of about 3 km probably occurred due to the activity of low-angle normal faults.

Microstructural analysis indicates that the mélangé initially formed under brittle conditions, with the development of a cataclastite (stage D_0), and subsequently under ductile conditions (stages D_1 - D_2 - D_3), leading to the formation of an early disjunctive cleavage (S_1), which was later transposed by a main crenulation cleavage (S_2). Both foliations consist of thin Wm and Chl assemblages. A third cleavage (S_3) is weakly developed. All meso- and microstructures indicate a tectonic vergence toward the E/SE. The strain and kinematic vorticity analyses provide valuable insights into the type of 3D deformation and the role of coaxial strain. The calculated finite strain ellipsoids are oblate, with the maximum stretching (X -axis) parallel to the shear direction. The estimated percentage of pure shear is in the range of 20%–35%.

These results provide a comprehensive overview of the tectonic, burial, and exhumation history of the Tempa Roccarossa mélangé and associated units. They emphasize the significant role of brittle deformation, which acted as a precursor to the subsequent ductile strain and unloading processes, such as near-surface low-angle normal faulting during in- and out-of-sequence thrusting pulses. This accounts for the thermal breaks between the different thrust sheets that form the southern Apennines fold-and-thrust belt. Finally, this work marks the importance of a detailed strain and kinematic analysis to fully characterize the tectonic mélanges and their evolution and a petrologic and mineralogic multi-approach to discriminate the role of detrital minerals from ones in equilibrium with the new P-T conditions, especially in low-grade metamorphic rocks, such as one analyzed in this work.

Data Availability Statement

Borehole data are from ViDEPi Project (2025). Data available online via <https://www.videpi.com/videpi/pozzi/pozzi.asp>. Geological maps are from Servizio Geologico d'Italia (1969) and ISPRA (2014). Geological maps are available online via <https://www.isprambiente.gov.it/en>. Other data used in this study are fully accessible through text, figures, and Supporting Information S1 and S2. Quantitative analysis on bulk sample XRD profiles was made by using the Winfit software (Krumm, 1999). The software is available online via <http://www.ccp14.ac.uk/ccp/web-mirrors/krumm/html/software/winsoft.html>. For the chlorite and white mica multi-equilibrium geothermobarometry we used the ChlMicaEqui 1.5 program (Lanari, 2012). The software information is available online via <https://pierrelanari.com/programs/>. For the strain analysis, we used the free software EllipseFit (Vollmer, 2018). The software is available online via <https://www.frederickvollmer.com/ellipsefit/index.html>. Stereographic projection plots were made by the free software Openstereo (Grohmann & Campanha, 2010). The software is available online via <https://igc.usp.br/openstereo/>.

References

- Alberti, M., Lapenta, M. C., & Maurella, A. (2001). New geological data on the basin units surrounding the Mount Alpi Unit (southern Italy). *Bollettino Società Naturalisti in Napoli-Nuova Serie*, 1, 85–96.
- Aldega, L., Corrado, S., Giampaolo, C., & Mazzoli, S. (2003). Studio della mineralogia delle argille per la ricostruzione dei carichi tettonico/sedimentari; esempi dalle Unità Lagonegresi e Liguridi della Lucania sud-occidentale (Appennino Meridionale). *Bollettino della Società Geologica Italiana*, 122(2), 203–216.
- Amodio-Morelli, L., Bonardi, G., Colonna, V., Dietrich, D., Giunta, G., Ippolito, F., et al. (1976). L'Arco Calabro-Peloritano nell'orogene appenninico-maghebide. *Memorie della Società Geologica Italiana*, 17, 1–60.
- Ascione, A., Mazzoli, S., Petrosino, P., & Valente, E. (2013). A decoupled kinematic model for active normal faults: Insights from the 1980, MS = 6.9 Irpinia earthquake, southern Italy. *Geological Society of America Bulletin*, 125(7–8), 1239–1259. <https://doi.org/10.1130/b30814.1>
- Barnes, P. M., & Korsch, R. J. (1991). Melange and related structures in Torlesse accretionary wedge, Wairarapa, New Zealand. *New Zealand Journal of Geology and Geophysics*, 34(4), 517–532. <https://doi.org/10.1080/00288306.1991.9514487>
- Beaufort, D., Rigault, C., Billon, S., Billault, V., Inoue, A., Inoue, S., & Patrier, P. (2015). Chlorite and chloritization processes through mixed-layer mineral series in low-temperature geological systems—a review. *Clay Minerals*, 50(4), 497–523. <https://doi.org/10.1180/claymin.2015.050.4.06>
- Behrmann, J. H. (1987). A precautionary note on shear bands as kinematic indicators. *Journal of Structural Geology*, 9(5–6), 659–666. [https://doi.org/10.1016/0191-8141\(87\)90150-7](https://doi.org/10.1016/0191-8141(87)90150-7)
- Berman, R. G. (1988). Internally-consistent thermodynamic data for minerals in the system Na₂O-K₂O-CaO-MgO-FeO-Fe₂O₃-Al₂O₃-SiO₂-TiO₂-H₂O-CO₂. *Journal of Petrology*, 29(2), 445–522. <https://doi.org/10.1093/petrology/29.2.445>
- Bons, P., & Montenari, M. (2005). The formation of antitaxial calcite veins with well-developed fibres, Oppaminda Creek, South Australia. *Journal of Structural Geology*, 27(2), 231–248. <https://doi.org/10.1016/j.jsg.2004.08.009>
- Bourdelle, F. (2021). Low-temperature chlorite geothermometry and related recent analytical advances: A review. *Minerals*, 11(2), 130. <https://doi.org/10.3390/min11020130>
- Bourdelle, F., & Cathelineau, M. (2015). Low-temperature chlorite geothermometry: A graphical representation based on a T-R₂+Si diagram. *European Journal of Mineralogy*, 27(5), 617–626. <https://doi.org/10.1127/ejm/2015/0027-2467>

Acknowledgments

We thank the Editor Laurent Jolivet, the Associate Editor Feng Cheng, two anonymous reviewers, and Alessandro Petrocchia for their suggestions, which have greatly improved this work. The authors also thank Sergio Bravi and Roberto de Gennaro for preparing the thin section and assisting with SEM-EDS microanalysis. Open access publishing facilitated by Università degli Studi di Napoli Federico II, as part of the Wiley - CRUI-CARE agreement.

- Brueckner, H. K., Lallemand, H. G. A., Sisson, V. B., Harlow, G. E., Hemming, S. R., Martens, U. T. T., & Sorensen, S. S. (2009). Metamorphic reworking of a high pressure–low temperature mélange along the Motagua fault, Guatemala: A record of Neocomian and Maastrichtian transpressional tectonics. *Earth and Planetary Science Letters*, *284*(1–2), 228–235.
- Butler, R. W. H., Mazzoli, S., Corrado, S., De Donatis, M., Di Bucci, D., Gambini, R., et al. (2004). Applying thick-skinned tectonic models to the Apennine thrust belt of Italy: Limitations and implications. *AAPG Memoir*, *83*, 647–667.
- Byrne, T. (1984). Early deformation in mélange terranes of the ghost rocks formation, Kodiak Islands, Alaska. In L. A. Raymond (Ed.), *Melanges: Their Nature, Origin and Significance* (pp. 21–51). Geological Society of America. (Special Paper 198).
- Cardello, G. L., Bernasconi, S. M., Fellin, M. G., Rahn, M., Roskopf, R., Maden, C., & Mancktelow, N. S. (2024). Carbonate deformation through the brittle-ductile transition: The case of the SW Helvetic nappes, Switzerland. *Journal of Structural Geology*, *181*, 105083. <https://doi.org/10.1016/j.jsg.2024.105083>
- Cardello, G. L., Di Vincenzo, G., Giorgetti, G., Zwingmann, H., & Mancktelow, N. (2019). Initiation and development of the Pennine basal thrust (Swiss Alps): A structural and geochronological study of an exhumed megathrust. *Journal of Structural Geology*, *126*, 338–356. <https://doi.org/10.1016/j.jsg.2019.06.014>
- Cardello, G. L., Vico, G., Consorti, L., Sabbatino, M., Carminati, E., & Doglioni, C. (2021). Constraining the passive to active margin tectonics of the internal central Apennines: Insights from biostratigraphy, structural, and seismic analysis. *Geosciences*, *11*(4), 160. <https://doi.org/10.3390/geosciences11040160>
- Casciello, E., Cesarano, M., & Pappone, G. (2006). Extensional detachment faulting on the Tyrrhenian margin of the southern Apennines contractional belt (Italy). *Journal of the Geological Society*, *163*(4), 617–629. <https://doi.org/10.1144/0016-764905-054>
- Catalano, S., Monaco, C., Tortorici, L., Paltrinieri, W., & Steel, N. (2004). Neogene-Quaternary tectonic evolution of the southern Apennines. *Tectonics*, *23*(2). <https://doi.org/10.1029/2003TC001512>
- Catalano, S., Torrisi, S., De Guidi, G., Grasso, G., Lanzafame, G., Romagnoli, G., et al. (2007). Sistema a pieghe tardo-quaternarie nell'area di Catania: un esempio di fronte orogenico attivo. *Rendiconti online della Società Geologica Italiana*, *4*, 181–183.
- Cavalcante, F., Belviso, C., Laurita, S., & Prosser, G. (2012). PT constraints from phyllosilicates of the Liguride Complex of the Pollino area (Southern Apennines, Italy): Geological inferences. *Ofioliti*, *37*(2), 65–75.
- Cavalcante, F., Fiore, S., Lettino, A., Piccarreta, G., & Tateo, F. (2007). Illite-Smectite mixed layer in Sicilide shales and piggy-back deposits of the Gorgoglione Formation (Southern Apennines): Geological inferences. *Bollettino della Società Geologica Italiana*, *126*, 241–254.
- Cavalcante, F., Perri, F., Belviso, C., Lettino, A., Prosser, G., La Bruna, V., & Agosta, F. (2023). Clayey sediments analysis as a useful tool to assessing the geodynamic evolution of fold-and-thrust belts: The case study of the Monte Alpi area (southern Apennines, Italy). *Marine and Petroleum Geology*, *151*, 106204. <https://doi.org/10.1016/j.marpetgeo.2023.106204>
- Cesarano, M., Bish, D. L., Cappelletti, P., Cavalcante, F., Belviso, C., & Fiore, S. (2018). Quantitative mineralogy of clay-rich siliciclastic landslide terrain of the Sorrento Peninsula, Italy, using a combined XRPD and XRF approach. *Clays and Clay Minerals*, *66*(4), 353–369. <https://doi.org/10.1346/ccmn.2018.064108>
- Chang, C. P., Angelier, J., & Lu, C. Y. (2009). Polyphase deformation in a newly emerged accretionary prism: Folding, faulting and rotation in the southern Taiwan Mountain range. *Tectonophysics*, *466*(3–4), 395–408. <https://doi.org/10.1016/j.tecto.2007.11.002>
- Ciarapica, G., & Passeri, L. (2000). The Lower and Middle Triassic facies (Monte Facito Auct. Formation) in the areas of Sasso di Castalda and Moliterno (Basilicata). *Bulletin of the Italian Geological Society*, *119*(2), 339–378.
- Ciarcia, S., & Vitale, S. (2025). Orogenic evolution of the northern Calabria-southern Apennines system in the framework of the Alpine chains in the central-Western Mediterranean area. *GSA Bull.*, *137*(3–4), 1143–1176. <https://doi.org/10.1130/B37474.1>
- Cloos, M. (1983). Comparative study of mélange matrix and metashales from the Franciscan subduction complex with the basal Great Valley sequence, California. *The Journal of Geology*, *91*(3), 291–306. <https://doi.org/10.1086/628772>
- Cloos, M. (1984). Flow melanges and the structural evolution of accretionary wedges. *Geological Society of America Special Paper*, *198*, 71–79.
- Cloos, M., & Shreve, R. L. (1988). Subduction channel model of prism accretion, mélange formation, sediment subduction, and subduction erosion at convergent plate margins; Part II, Implications and discussion. *Pure and Applied Geophysics*, *128*(3–4), 501–545. <https://doi.org/10.1007/bf00874549>
- Codegone, G., Festa, A., & Dilek, Y. (2012). Formation of Taconic mélanges and broken formations in the Hamburg Klippe, central Appalachian orogenic belt, eastern Pennsylvania. *Tectonophysics*, *568*, 215–229.
- Corrado, S., Invernizzi, C., & Mazzoli, S. (2002). Tectonic burial and exhumation in a foreland fold and thrust belt: The Monte Alpi case history (Southern Apennines, Italy). *Geodinamica Acta*, *15*(3), 159–177. <https://doi.org/10.1080/09853111.2002.10510750>
- Cowan, D. S. (1985). Structural styles in Mesozoic and Cenozoic mélanges in the Western Cordillera of North America. *Geological Society of America Bulletin*, *96*(4), 451–462. [https://doi.org/10.1130/0016-7606\(1985\)96<451:ssimac>2.0.co;2](https://doi.org/10.1130/0016-7606(1985)96<451:ssimac>2.0.co;2)
- Doglioni, C. (1991). A proposal for the kinematic modelling of W-dipping subductions-possible applications to the Tyrrhenian-Apennines system. *Terra Nova*, *3*(4), 423–434. <https://doi.org/10.1111/j.1365-3121.1991.tb00172.x>
- Dubacq, B., Vidal, O., & De Andrade, V. (2010). Dehydration of dioctahedral aluminous phyllosilicates: Thermodynamic modelling and implications for thermobarometric estimates. *Contributions to Mineralogy and Petrology*, *159*(2), 159–174. <https://doi.org/10.1007/s00410-009-0421-6>
- Dunnet, D. (1969). A technique of finite strain analysis using elliptical particles. *Tectonophysics*, *7*(2), 117–136. [https://doi.org/10.1016/0040-1951\(69\)90002-x](https://doi.org/10.1016/0040-1951(69)90002-x)
- Elliott, W. C., & Matisoff, G. (1996). Evaluation of kinetic models for the smectite to illite transformation. *Clays and Clay Minerals*, *44*(1), 77–87. <https://doi.org/10.1346/ccmn.1996.0440107>
- Escuder-Viruete, J., Pérez-Estaún, A., Booth-Rea, G., & Valverde-Vaquero, P. (2011). Tectonometamorphic evolution of the Samaná complex, northern Hispaniola: Implications for the burial and exhumation of high-pressure rocks in a collisional accretionary wedge. *Lithos*, *125*, 190–210. <https://doi.org/10.1016/j.lithos.2011.02.006>
- Evans, B. W. & Brown, E. H. (Eds.) (1986). *Blueschists and eclogites* (Vol. 164). Geological Society of America Memoir.
- Federico, L., Crispini, L., Scambelluri, M., & Capponi, G. (2007). Ophiolite mélange zone records exhumation in a fossil subduction channel. *Geology*, *35*(6), 499–502. <https://doi.org/10.1130/g23190a.1>
- Fernandez, G., Costa, A., Giaccio, B., Natale, J., Palladino, D. M., & Sottili, G. (2025). The Maddaloni/X-6 eruption stands out as one of the major events during the Late Pleistocene at Campi Flegrei. *Communications Earth & Environment*, *6*(1), 27. <https://doi.org/10.1038/s43247-025-01998-8>
- Ferranti, L., & Oldow, J. S. (1999). History and tectonic implications of low-angle detachment faults and orogen parallel extension, Picentini Mountains, Southern Apennines fold and thrust belt, Italy. *Tectonics*, *18*(3), 498–526. <https://doi.org/10.1029/1998tc900024>
- Festa, A., Dilek, Y., Pini, G. A., Codegone, G., & Ogata, K. (2012). Mechanisms and processes of stratal disruption and mixing in the development of mélanges and broken formations: Redefining and classifying mélanges. *Tectonophysics*, *568*, 7–24.

- Festa, A., Pini, G. A., Dilek, Y., & Codegone, G. (2010). Mélanges and mélange-forming processes: A historical overview and new concepts. *International Geology Review*, 52(10–12), 1040–1105. <https://doi.org/10.1080/00206810903557704>
- Festa, A., Pini, G. A., Ogata, K., & Dilek, Y. (2019). Diagnostic features and field-criteria in recognition of tectonic, sedimentary and diapiric mélanges in orogenic belts and exhumed subduction-accretion complexes. *Gondwana Research*, 74, 7–30. <https://doi.org/10.1016/j.gr.2019.01.003>
- Fisher, D., & Byrne, T. (1987). Structural evolution of underthrust sediments, Kodiak Islands, Alaska. *Tectonics*, 6, 775–793. <https://doi.org/10.1029/tc006i006p00775>
- Flinn, D. (1962). On folding during three-dimensional progressive deformation. *Quarterly Journal of the Geological Society of London*, 118(1–4), 385–433. <https://doi.org/10.1144/gsjgs.118.1.0385>
- Forshaw, J. B., & Pattison, D. R. M. (2023). Major-element geochemistry of pelites. *Geology*, 51(1), 39–43. <https://doi.org/10.1130/G50542.1>
- Fossen, H., & Cavalcante, G. C. G. (2017). Shear zones—A review. *Earth-Science Reviews*, 171, 434–455. <https://doi.org/10.1016/j.earscirev.2017.05.002>
- Fukui, A., & Kano, K. (2007). Deformation process and kinematics of mélange in the Early Cretaceous accretionary complex of the Mino-Tamba Belt, eastern southwest Japan. *Tectonics*, 26(2), TC2006. <https://doi.org/10.1029/2006TC001945>
- García-Castellanos, D., & Villaseñor, A. (2011). Messinian salinity crisis regulated by competing tectonics and erosion at the Gibraltar arc. *Nature*, 480(7377), 359–363. <https://doi.org/10.1038/nature10651>
- Gillam, B. G., Little, T. A., Smith, E., & Toy, V. G. (2013). Extensional shear band development on the outer margin of the Alpine mylonite zone, Tareare Stream, Southern Alps, New Zealand. *Journal of Structural Geology*, 54, 1–20. <https://doi.org/10.1016/j.jsg.2013.06.010>
- Graessner, T., & Schenk, V. (1999). Low-pressure metamorphism of Palaeozoic pelites in the Aspromonte, southern Calabria: Constraints for the thermal evolution in the Calabrian crustal cross-section during the Hercynian orogeny. *Journal of Metamorphic Geology*, 17(2), 157–172. <https://doi.org/10.1046/j.1525-1314.1999.00188.x>
- Graham, C. M., & England, P. C. (1976). Thermal regimes and regional metamorphism in the vicinity of overthrust faults: An example of shear heating and inverted metamorphic zonation from southern California. *Earth and Planetary Science Letters*, 31(1), 142–152. [https://doi.org/10.1016/0012-821x\(76\)90105-9](https://doi.org/10.1016/0012-821x(76)90105-9)
- Grasemann, B., & Stüwe, K. (2001). The development of flanking folds during simple shear and their use as kinematic indicators. *Journal of Structural Geology*, 23(4), 715–724. [https://doi.org/10.1016/s0191-8141\(00\)00108-5](https://doi.org/10.1016/s0191-8141(00)00108-5)
- Grohmann, C. H., & Campanha, G. A. C. (2010). OpenStereo: Open source, cross-platform software for structural geology analysis [Software]. In *Presented at the AGU 2010 Fall Meeting, San Francisco, CA*. Retrieved from <https://fig.usp.br/openstereo/>
- Guidotti, C. V., & Sassi, F. P. (1998). Petrogenetic significance of Na–K white mica mineralogy: Recent advances for metamorphic rocks. *European Journal of Mineralogy*, 10(5), 815–854. <https://doi.org/10.1127/ejm/10/5/0815>
- Guyett, P. C., Chew, D., Azevedo, V., Blennerhassett, L. C., Rosca, C., & Tomlinson, E. (2024). Optimizing SEM-EDX for fast, high-quality and non-destructive elemental analysis of glass. *Journal of Analytical Atomic Spectrometry*, 39(10), 2565–2579. <https://doi.org/10.1039/D4JA00212A>
- Hammond, R. L. (1987). The influence of deformation partitioning on dissolution and solution transfer in low-grade tectonic mélange. *Journal of Metamorphic Geology*, 5(2), 195–211. <https://doi.org/10.1111/j.1525-1314.1987.tb00379.x>
- Herron, M. M. (1988). Geochemical classification of terrigenous sands and shales from core or log data. *Journal of Sedimentary Petrology*, 58, 820–829.
- Hey, M. H. (1954). A new review of the chlorites. *Mineralogical Magazine*, 30(224), 277–292. <https://doi.org/10.1180/minmag.1954.030.224.01>
- Hsü, K. J. (1968). Principles of mélanges and their bearing on the Franciscan-Knoxville paradox. *Geological Society of America Bulletin*, 79(8), 1063–1074. [https://doi.org/10.1130/0016-7606\(1968\)79\[1063:pomath\]2.0.co;2](https://doi.org/10.1130/0016-7606(1968)79[1063:pomath]2.0.co;2)
- Huang, C. Y., Yuan, P. B., & Tsao, S. J. (2006). Temporal and spatial records of active arc-continent collision in Taiwan: A synthesis. *Geological Society of America Bulletin*, 118(3–4), 274–288. <https://doi.org/10.1130/b25527.1>
- Iacopini, D., Frassi, C., Carosi, R., & Montomoli, C. (2011). Biases in three-dimensional vorticity analysis using porphyroclast system: Limits and application to natural examples. *Geological Society - Special Publications*, 360(1), 301–318. <https://doi.org/10.1144/sp360.17>
- Iannace, A., Vitale, S., D'errico, M., Mazzoli, S., Di Staso, A., Macaione, E., et al. (2007). The carbonate tectonic units of northern Calabria (Italy): A record of Apulian palaeomargin evolution and Miocene convergence, continental crust subduction, and exhumation of HP–LT rocks. *Journal of the Geological Society*, 164(6), 1165–1186. <https://doi.org/10.1144/0016-76492007-017>
- ISPRA. (2014). Geological maps of Italy, scale 1:50,000. Sheet 521 Lauria [Dataset]. *ISPRA*. Retrieved from https://www.isprambiente.gov.it/Media/carg/521_LAURIA/Foglio.html
- Jessup, M. J., Law, R. D., & Frassi, C. (2007). The rigid grain net (RGN): An alternative method for estimating mean kinematic vorticity number (Wm). *Journal of Structural Geology*, 29(3), 411–421. <https://doi.org/10.1016/j.jsg.2006.11.003>
- Kimura, G., Hina, S., Hamada, Y., Kameda, J., Tsuji, T., Kinoshita, M., & Yamaguchi, A. (2012). Runaway slip to the trench due to rupture of highly pressurized megathrust beneath the middle trench slope: The tsunamigenesis of the 2011 Tohoku earthquake off the East Coast of northern Japan. *Earth and Planetary Science Letters*, 339, 32–45. <https://doi.org/10.1016/j.epsl.2012.04.002>
- Kisch, H. J. (1987). Correlation between indicators of very low-grade metamorphism. In M. Frey (Ed.), *Low temperature metamorphism* (pp. 227–300). Blackie.
- Kitamura, Y., Sato, K., Ikesawa, E., Ikehara-Ohmori, K., Kimura, G., Kondo, H., et al. (2005). Mélange and its seismogenic roof décollement: A plate boundary fault rock in the subduction zone—An example from the Shimanto belt, Japan. *Tectonics*, 24(5). <https://doi.org/10.1029/2004tc001635>
- Krumm, S. (1999). The Erlangen geological and mineralogical software collection [Software]. *Computers & Geosciences*, 25(4), 489–499. [https://doi.org/10.1016/s0098-3004\(98\)00154-x](https://doi.org/10.1016/s0098-3004(98)00154-x)
- Kuehn, S. C., Froese, D. G., Shane, P. A. R., & INTAV Intercomparison Participants. (2011). The INTAV intercomparison of electron-beam microanalysis of glass by tephrochronology laboratories: Results and recommendations. *Quaternary International*, 246(1–2), 19–47. <https://doi.org/10.1016/j.quaint.2011.08.022>
- Kurz, G. A., & Northrup, C. J. (2008). Structural analysis of mylonitic rocks in the Cougar Creek Complex, Oregon–Idaho using the porphyroclast hyperbolic distribution method, and potential use of SC⁺-type extensional shear bands as quantitative vorticity indicators. *Journal of Structural Geology*, 30(8), 1005–1012. <https://doi.org/10.1016/j.jsg.2008.04.003>
- La Bruna, V., Agosta, F., Lamarche, J., Viseur, S., & Prosser, G. (2018). Fault growth mechanisms and scaling properties in foreland basin system: The case study of Monte Alpi, Southern Apennines, Italy. *Journal of Structural Geology*, 116, 94–113. <https://doi.org/10.1016/j.jsg.2018.08.009>
- Lanari, P. (2012). Micro-cartographie PT- dans les roches métamorphiques. Applications aux Alpes et à l'Himalaya. ChlMicaEqui 1.5 program [Software]. *Doctoral dissertation, Université de Grenoble*, 534. <https://pierrelanari.com/programs/>

- Lanari, P., & Duisterhoeft, E. (2019). Modelling metamorphic rocks using equilibrium thermodynamics and internally consistent databases: Past achievements, problems and perspectives. *Journal of Petrology*, 60(1), 19–56. <https://doi.org/10.1093/ptrology/egy105>
- Lanari, P., Guillot, S., Schwartz, S., Vidal, O., Tricart, P., Riel, N., & Beyssac, O. (2012). Diachronous evolution of the alpine continental subduction wedge: Evidence from P-T estimates in the Briançonnais Zone houillère (France – Western Alps). *Journal of Geodynamics*, 56–57, 39–54. <https://doi.org/10.1016/j.jog.2011.09.006>
- Leoni, L., Lezzerini, M., & Saitta, M. (2008). Calcolo computerizzato dell'analisi mineralogica quantitativa di rocce e sedimenti argillosi basato Sulla combinazione dei dati chimici e diffrattometrici. *Atti della Società Toscana delle Scienze Naturali di Pisa, Serie A*, 113, 63–69.
- Leoni, L., Marroni, M., Sartori, F., & Tamponi, M. (1996). Metamorphic grade in metapelites of the Internal Liguride Units (northern Apennines, Italy). *European Journal of Mineralogy*, 8(1), 35–50. <https://doi.org/10.1127/ejm/8/1/0035>
- Lustrino, M., Morra, V., Fedele, L., & Franciosi, L. (2009). The beginning of the Apennine subduction system in central-Western Mediterranean: Constraints from Cenozoic orogenic magmatic activity of Sardinia (Italy). *Tectonics*, 28(5), TC5016. <https://doi.org/10.1029/2008tc002419>
- Maino, M., Casini, L., Boschi, C., Di Giulio, A., Setti, M., & Seno, S. (2020). Time-dependent heat budget of a thrust from geological records and numerical experiments. *Journal of Geophysical Research: Solid Earth*, 125(3), e2019JB018940. <https://doi.org/10.1029/2019jb018940>
- Mancktelow, N. S., & Pennacchioni, G. (2005). The control of precursor brittle fracture and fluid-rock interaction on the development of single and paired ductile shear zones. *Journal of Structural Geology*, 27(4), 645–661. <https://doi.org/10.1016/j.jsg.2004.12.001>
- Mattioni, L., Shiner, P., Tondi, E., Vitale, S., & Cello, G. (2006). The Argille Varicolori Unit of Lucania (Italy): A record of tectonic offscraping and gravity sliding in the Mesozoic-Tertiary Lagonegro basin, southern Apennines. In G. Moratti & A. Chalouan (Eds.) *Geology and Active Tectonics of the Western Mediterranean Region and North Africa* (Vol. 262, pp. 277–288). Special Publication of the Geological Society. <https://doi.org/10.1144/GSL.SP.2006.262.01.17>
- Mazzoli, S. (1992). Structural analysis of the Mesozoic Lagonegro Units in SW Lucania. (Southern Italian Apennines). *Studi Geologici Camerti*, 12, 117–146.
- Mazzoli, S. (1995). Strain analysis in Jurassic argillites of the Monte Sirino area (Lagonegro Zone, southern Apennines, Italy) and implications for deformation paths in pelitic rocks. *Geologische Rundschau*, 84(4), 781–793. <https://doi.org/10.1007/bf00240568>
- Mazzoli, S., Aldega, L., Corrado, S., Invernizzi, C., & Zattin, M. (2006). Pliocene-quaternary thrusting, syn-orogenic extension and tectonic exhumation in the Southern Apennines (Italy): Insights from the Monte Alpi area. In S. Mazzoli & R. W. H. Butler (Eds.), *Styles of continental contraction* (Vol. 414, pp. 55–77). Geological Society of America, Spec. Paper. [https://doi.org/10.1130/2006.2414\(04\)](https://doi.org/10.1130/2006.2414(04))
- Mazzoli, S., Ascione, A., Candela, S., Iannace, A., Megna, A., Santini, S., & Vitale, S. (2013). Subduction and continental collision events in the southern Apennines: Constraints from two crustal cross-sections. *Rendiconti online della Società Geologica Italiana*, 25, 78–84.
- Mazzoli, S., Barkham, S., Cello, G., Gambini, R., Mattioni, L., Shiner, P., & Tondi, E. (2001). Reconstruction of continental margin architecture deformed by the contraction of the Lagonegro Basin, southern Apennines, Italy. *Journal of the Geological Society*, 158(2), 309–319. <https://doi.org/10.1144/jgs.158.2.309>
- Mazzoli, S., D'errico, M., Aldega, L., Corrado, S., Invernizzi, C., Shiner, P., & Zattin, M. (2008). Tectonic burial and “young” (<10 Ma) exhumation in the southern Apennines fold-and-thrust belt (Italy). *Geology*, 36(3), 243–246. <https://doi.org/10.1130/g24344a.1>
- Mazzoli, S., Zampetti, V., & Zuppetta, A. (2001). Very low temperature, natural deformation of fine grained limestone: A case study from the Lucania region, southern Apennines, Italy. *Geodinamica Acta*, 14(4), 213–230. <https://doi.org/10.1080/09853111.2001.11432445>
- Means, W. D., Hobbs, B. E., Lister, G. S., & Williams, P. F. (1980). Vorticity and non-coaxiality in progressive deformations. *Journal of Structural Geology*, 2(3), 371–378. [https://doi.org/10.1016/0191-8141\(80\)90024-3](https://doi.org/10.1016/0191-8141(80)90024-3)
- Means, W. D., & Park, Y. (1994). New experimental approach to understanding igneous texture. *Geology*, 22(4), 323–326. [https://doi.org/10.1130/0091-7613\(1994\)022<0323:neatui>2.3.co;2](https://doi.org/10.1130/0091-7613(1994)022<0323:neatui>2.3.co;2)
- Megna, A., Candela, S., Mazzoli, S., & Santini, S. (2014). *An analytical model for the geotherm in the Basilicata oil fields area (southern Italy)*. (Vol. 133, pp. 204–213). Italian Journal of Geosciences. <https://doi.org/10.13301/IJG.2014.02>
- Montemagni, C., Carosi, R., Fusi, N., Iaccarino, S., Montomoli, C., Villa, I. M., & Zanchetta, S. (2020). Three-dimensional vorticity and time-constrained evolution of the main central thrust zone, Garhwal Himalaya (NW India). *Terra Nova*, 32(3), 215–224. <https://doi.org/10.1111/ter.12450>
- Moore, D. M., & Reynolds, R. C., Jr. (1997). *X-ray diffraction and the identification and analysis of clay minerals* (2nd ed., p. 378). Oxford University Press.
- Mori, H., Wallis, S., Fujimoto, K., & Shigematsu, N. (2015). Recognition of shear heating on a long-lived major fault using Raman carbonaceous material thermometry: Implications for strength and displacement history of the MTL, SW Japan. *Island Arc*, 24(4), 425–446. <https://doi.org/10.1111/iar.12129>
- Needham, D. T. (1995). Mechanisms of mélange formation: Examples from SW Japan and southern Scotland. *Journal of Structural Geology*, 17(7), 971–985. [https://doi.org/10.1016/0191-8141\(94\)00132-j](https://doi.org/10.1016/0191-8141(94)00132-j)
- Novellino, R., Prosser, G., Bucci, F., Tavarnelli, E., Abdallah, I., & Agosta, F. (2025). Structural architecture and micromechanics of the carbonate-hosted low-angle normal fault, Agri Valley, southern Apennines, Italy. *Journal of Structural Geology*, 192, 105352. <https://doi.org/10.1016/j.jsg.2025.105352>
- Ogata, K., Festa, A., Pini, G. A., Pogačnik, Ž., & Lucente, C. C. (2019). Substrate deformation and incorporation in sedimentary mélanges (olistostromes): Examples from the northern Apennines (Italy) and northwestern Dinarides (Slovenia). *Gondwana Research*, 74, 101–125. <https://doi.org/10.1016/j.gr.2019.03.001>
- Ogawa, Y., Anma, R., & Dilek, Y. (Eds.) (2011). *Accretionary Prisms and Convergent Margin Tectonics in the Northwest Pacific Basin* (Vol. 8). Springer Science & Business Media.
- Parra, T., Vidal, O., & Agard, P. (2002). A thermodynamic model for Fe–Mg dioctahedral K white micas using data from phase-equilibrium experiments and natural pelitic assemblages. *Contributions to Mineralogy and Petrology*, 143(6), 706–732. <https://doi.org/10.1007/s00410-002-0373-6>
- Passchier, C. W., & Trouw, R. A. J. (2005). *Microtectonics*. Springer-Verlag.
- Passeri, L., & Ciarapica, G. (2010). Le litofacies permiane e triassiche Della Formazione di M. Facito auctt. nell'area di M. Facito (successione di Lagonegro, Appennino meridionale). *Italian Journal of Geosciences*, 129(1), 29–50. <https://doi.org/10.3301/IJG.2009.05>
- Patacca, E., & Scandone, P. (2007). Geology of southern Apennines. In A. Mazzotti, E. Patacca, & P. Scandone (Eds.), *Results of the CROP Project, Sub-Project CROP-04* (Vol. 7, pp. 75–119). Bollettino della Società Geologica Italiana, Special Issue.
- Pennacchioni, G., & Mancktelow, N. S. (2007). Nucleation and initial growth of a shear zone network within compositionally and structurally heterogeneous granitoids under amphibolite facies conditions. *Journal of Structural Geology*, 29(11), 1757–1780. <https://doi.org/10.1016/j.jsg.2007.06.002>
- Penniston-Dorland, S. C., & Harvey, K. M. (2023). Constraints on tectonic processes in subduction mélange: A review of insights from the Catalina Schist (CA, USA). *Geosystems and Geoenvironment*, 2(3), 100190. <https://doi.org/10.1016/j.geogeo.2023.100190>

- Petroccia, A., Carosi, R., Montomoli, C., Iaccarino, S., & Vitale Brovarone, A. (2022). Thermal variation across collisional orogens: Insights from the hinterland-foreland transition zone of the Sardinian Variscan belt. *Terra Nova*, 35(2), 113–123. <https://doi.org/10.1111/ter.12635>
- Petroccia, A., Forshaw, J. B., Lanari, P., Iaccarino, S., Montomoli, C., & Carosi, R. (2025). Pressure and temperature estimation in greenschist-facies metapelites: An example from the Variscan belt in Sardinia. *Journal of Metamorphic Geology*, 43(1), 21–46. <https://doi.org/10.1111/jmg.12799>
- Platt, J. P., & Vissers, R. L. M. (1980). Extensional structures in anisotropic rocks. *Journal of Structural Geology*, 2(4), 397–410. [https://doi.org/10.1016/0191-8141\(80\)90002-4](https://doi.org/10.1016/0191-8141(80)90002-4)
- Ramsay, J. G. (1967). *Folding and fracturing of rocks* (p. 568). McGraw Hill.
- Ramsay, J. G., & Huber, M. (1983). *The techniques of modern structural geology: Strain analysis* (Vol. I). Academic Press.
- Richter, M., Pollok, K., Onuzi, K., & Ustaszewski, K. (2025). Tectonometamorphic evolution of a subduction plate interface at the base of the Mirdita Ophiolite (Bajram Curri, northeastern Albania). *Swiss Journal of Geosciences*, 118(1), 4. <https://doi.org/10.1186/s00015-024-00472-5>
- Rinaldi, A. P., Improta, L., Hainzl, S., Catalli, F., Urpi, L., & Wiemer, S. (2020). Combined approach of poroelastic and earthquake nucleation applied to the reservoir-induced seismic activity in the Val d'Agri area, Italy. *Journal of Rock Mechanics and Geotechnical Engineering*, 12(4), 802–810. <https://doi.org/10.1016/j.jrmge.2020.04.003>
- Robinson, D., Schmidt, S. T., Zamora, D., & Santana, A. (2002). Reaction pathways and reaction progress for the smectite-to-chlorite transformation: Evidence from hydrothermally altered metabasites. *Journal of Metamorphic Geology*, 20, 167–174.
- Roda, M., Zucali, M., Regorda, A., & Spalla, M. I. (2020). Formation and evolution of a subduction-related mélange: The example of the Rocca Canavese thrust sheets (Western Alps). *Geological Society of America Bulletin*, 132(3–4), 884–896. <https://doi.org/10.1130/b35213.1>
- Roure, F., Casero, P., & Vially, R. (1991). Growth processes and mélange formation in the southern Apennines accretionary wedge. *Earth and Planetary Science Letters*, 102(3–4), 395–412. [https://doi.org/10.1016/0012-821x\(91\)90031-c](https://doi.org/10.1016/0012-821x(91)90031-c)
- Rudnick, R. L., & Gao, S. (2014). Composition of the continental crust. In H. D. Holland & K. K. Turekian (Eds.), *Treatise on Geochemistry, The crust* (2nd ed., p. 4). Elsevier. <https://doi.org/10.1016/B978-0-08-095975-7.00301-6>
- Santangelo, N., Romano, P., Ascione, A., & Russo Ermolli, E. (2017). Quaternary evolution of the southern Apennines coastal plains: A review. *Geologica Carpathica*, 68(1), 43–56. <https://doi.org/10.1515/geoca-2017-0004>
- Scandone, P., Sgrosso, I., & Vallario, A. (1967). Finestra tettonica nella serie calcareo-silico-marnosa lucana presso Campagna (Monti Picentini, Salerno). *Bollettino Società Naturalisti in Napoli*, 76, 3–10.
- Schenk, V. (1980). U-Pb and Rb-Sr radiometric dates and their correlation with metamorphic events in the granulite facies basement of the Serre, southern Calabria (Italy). *Contributions to Mineralogy and Petrology*, 73(1), 23–38. <https://doi.org/10.1007/bf00376258>
- Schiattarella, M., Giano, S. I., & Gioia, D. (2017). Long-term geomorphological evolution of the axial zone of the Campania-Lucania Apennine, southern Italy: A review. *Geologica Carpathica*, 68(1), 57–67. <https://doi.org/10.1515/geoca-2017-0005>
- Schiattarella, M., Leo, P. D., Beneduce, P., Giano, S. I., & Martino, C. (2006). Tectonically driven exhumation of a young orogen: An example from the Southern Apennines, Italy. In S. D. Willett, N. Hovius, M. T. Brandon, & D. Fisher (Eds.), *Tectonics, climate, and landscape evolution* (Vol. 398, pp. 371–385). Special paper of the Geological Society of America.
- Schirripa Spagnolo, G. S., Agosta, F., Aldega, L., Prosser, G., Smeraglia, L., Tavani, S., et al. (2024). Structural architecture and maturity of Val d'Agri faults, Italy: Inferences from natural and induced seismicity. *Journal of Structural Geology*, 180, 105084. <https://doi.org/10.1016/j.jsg.2024.105084>
- Sciamanna, S., Sassi, W., Gambini, R., Rudkiewicz, J. L., Mosca, F., & Nicolai, C. (2004). Predicting hydrocarbon generation and expulsion in the southern Apennines thrust belt by 2-D integrated structural and geochemical modeling: Part I. Structural and thermal evolution. In R. Swennen, F. Roure, & J. W. Granath (Eds.), *Deformation, fluid flow, and reservoir appraisal in foreland fold and thrust belts (Series 1, 51–67)*. AAPG. Servizio Geologico d'Italia. (1969). Carta Geologica d'Italia alla scala 1:100.000, F. 210 Lauria [Dataset]. *Servizio Geologico d'Italia*. Retrieved from https://sgi.isprambiente.it/geologia100k/mostra_foglio.aspx?numero_foglio=210
- Srodon, J. (1999). Nature of mixed-layer clays and mechanisms of their formation and alteration. *Annual Review of Earth and Planetary Sciences*, 27(1), 19–53. <https://doi.org/10.1146/annurev.earth.27.1.19>
- Srodon, J., Drits, V. A., McCarty, D. K., Hsieh, J. C., & Eberl, D. D. (2001). Quantitative X-ray diffraction analysis of clay-bearing rocks from random preparations. *Clays and Clay Minerals*, 49(6), 514–528. <https://doi.org/10.1346/ccmn.2001.0490604>
- Tikoff, B., & Fossen, H. (1995). The limitations of three-dimensional kinematic vorticity analysis. *Journal of Structural Geology*, 17(12), 1771–1784. [https://doi.org/10.1016/0191-8141\(95\)00069-p](https://doi.org/10.1016/0191-8141(95)00069-p)
- Tikoff, B., & Fossen, H. (1999). Three-dimensional reference deformations and strain facies. *Journal of Structural Geology*, 21(11), 1497–1512. [https://doi.org/10.1016/s0191-8141\(99\)00085-1](https://doi.org/10.1016/s0191-8141(99)00085-1)
- van de Kamp, P. C. (2008). Smectite-illite-muscovite transformations, quartz dissolution, and silica release in shales. *Clays and Clay Minerals*, 56(1), 66–81. <https://doi.org/10.1346/ccmn.2008.0560106>
- Van Dijk, J. P., Bello, M., Brancaloni, G. P., Cantarella, G., Costa, V., Frixia, A., et al. (2000). A regional structural model for the northern sector of the Calabrian Arc (southern Italy). *Tectonophysics*, 324(4), 267–320. [https://doi.org/10.1016/s0040-1951\(00\)00139-6](https://doi.org/10.1016/s0040-1951(00)00139-6)
- Vidal, O., De Andrade, V., Lewin, E., Munoz, M., Parra, T., & Pascarelli, S. (2006). P-T-deformation-Fe³⁺/Fe²⁺ mapping at the thin section scale and comparison with XANES mapping: Application to a garnet-bearing metapelite from the Sambagawa metamorphic belt (Japan). *Journal of Metamorphic Geology*, 24(7), 669–683. <https://doi.org/10.1111/j.1525-1314.2006.00661.x>
- Vidal, O., & Parra, T. (2000). Exhumation paths of high pressure metapelites obtained from local equilibria for chlorite-phengite assemblages. *Geological Journal*, 35(3–4), 139–161. <https://doi.org/10.1002/gj.856>
- Vidal, O., Parra, T., & Vieillard, P. (2005). Thermodynamic properties of the tschermak solid solution in Fe-chlorite: Application to natural examples and possible role of oxidation. *American Mineralogist*, 90(2–3), 347–358. <https://doi.org/10.2138/am.2005.1554>
- ViDEPi Project. (2025). Visibility of petroleum exploration data in Italy [Dataset]. *ViDEPi Project*. Retrieved from <https://www.videpi.com/videpi/pozzi/pozzi.asp>
- Vissers, R. L., Strating, E. H. H., Heijmans, M., & Krabbendam, M. (2001). Structures and microstructures in a thrust-related, greenschist facies tectonic mélange, Voltri Group (NW Italy). *Ophioliti*, 26(1), 33–46.
- Vitale, S., & Ciarcia, S. (2018). Tectono-stratigraphic setting of the Campania region (southern Italy). *Journal of Maps*, 14(2), 9–21. <https://doi.org/10.1080/17445647.2018.1424655>
- Vitale, S., & Ciarcia, S. (2022). The dismembering of the Adria platforms following the late Cretaceous-Eocene abortive rift: A review of the tectono-stratigraphic record in the southern Apennines. *International Geology Review*, 64(20), 2866–2889. <https://doi.org/10.1080/00206814.2021.2004559>
- Vitale, S., Ciarcia, S., Fedele, L., & Tramparulo, F. D. (2019). The Ligurian oceanic successions in southern Italy: The key to decrypting the first orogenic stages of the southern Apennines-Calabria chain system. *Tectonophysics*, 750, 243–261. <https://doi.org/10.1016/j.tecto.2018.11.010>

- Vitale, S., Ciarcia, S., & Tramparulo, F. D. A. (2013). Deformation and stratigraphic evolution of the Ligurian accretionary complex in the southern Apennines (Italy). *Journal of Geodynamics*, 66, 120–133. <https://doi.org/10.1016/j.jog.2013.02.008>
- Vitale, S., Fedele, L., Tramparulo, F. D. A., Ciarcia, S., Mazzoli, S., & Novellino, A. (2013). Structural and petrological analyses of the Frido Unit (southern Italy): New insights into the early tectonic evolution of the southern Apennines-Calabrian arc system. *Lithos*, 168–169, 219–235. <https://doi.org/10.1016/j.lithos.2013.02.006>
- Vitale, S., & Mazzoli, S. (2009). Finite strain analysis of a natural ductile shear zone in limestones: Insights into 3-D coaxial vs. non-coaxial deformation partitioning. *Journal of Structural Geology*, 31(1), 104–113. <https://doi.org/10.1016/j.jsg.2008.10.011>
- Vitale, S., Prinzi, E. P., Ciarcia, S., Sabbatino, M., Tramparulo, F. D. A., & Verazzo, G. (2019). Polyphase out-of-sequence thrusting and occurrence of marble detritus within the wedge-top basin deposits in the Mt. Massico (southern Apennines): Insights into the late Miocene tectonic evolution of the central Mediterranean. *International Journal of Earth Sciences*, 108(2), 501–519. <https://doi.org/10.1007/s00531-018-1664-0>
- Vitale, S., Prinzi, E. P., Tramparulo, F. D. A., De Paola, C., Di Maio, R., Piegari, E., et al. (2020). Late Miocene-early Pliocene out-of-sequence thrusting in the southern Apennines (Italy). *Geosciences*, 10(8), 301. <https://doi.org/10.3390/geosciences10080301>
- Vitale, S., Tramparulo, F. D., Cappuccio, F., & Ciarcia, S. (2020). Brittle vs. ductile strain during the synorogenic exhumation of HP-LT rocks: An example from the Lungro-Verbicaro Unit mylonites (northern Calabria, Italy). *Journal of Geodynamics*, 135, 101719. <https://doi.org/10.1016/j.jog.2020.101719>
- Vitale, S., Zaghoul, M. N., El Ouaragli, B., Tramparulo, F. D., & Ciarcia, S. (2015). Polyphase deformation of the Dorsale Calcaire complex and the Maghrebien Flysch Basin units in the Jebha area (central Rif, Morocco): New insights into the Miocene tectonic evolution of the central Rif belt. *Journal of Geodynamics*, 90, 14–31. <https://doi.org/10.1016/j.jog.2015.07.002>
- Vollmer, F. W. (2018). Automatic contouring of geologic fabric and finite strain data on the unit hyperboloid [Software]. *Computers & Geosciences*, 115, 134–142. <https://doi.org/10.1016/j.cageo.2018.03.006>
- Waliczek, M., Machowski, G., Poprawa, P., Świerczewska, A., & Więclaw, D. (2021). A novel VRo, Tmax, and S indices conversion formulae on data from the fold-and-thrust belt of the Western Outer Carpathians (Poland). *International Journal of Coal Geology*, 234, 103672. <https://doi.org/10.1016/j.coal.2020.103672>
- Wallis, S. R., Platt, J. P., & Knott, S. D. (1993). Recognition of synconvergence extension in accretionary wedges with examples from the Calabrian Arc and the Eastern Alps. *American Journal of Science*, 293(5), 463–495. <https://doi.org/10.2475/ajs.293.5.463>
- Wang, J. P., Kusky, T. M., Polat, A., Wang, L., Deng, H., & Wang, S. J. (2013). A late Archean tectonic mélange in the central orogenic belt, North China Craton. *Tectonophysics*, 608, 929–946. <https://doi.org/10.1016/j.tecto.2013.07.025>
- Warr, L. N. (2018). A new collection of clay mineral “crystallinity” index standards and revised guidelines for the calibration of Kübler and Árkai indices. *Clay Minerals*, 53, 1–12.
- Warr, L. N., & Ferreiro Mählmann, R. (2015). Recommendations for Kübler index standardization. *Clay Minerals*, 50, 283–286.
- Warr, L. N., & Rice, A. H. N. (1994). Interlaboratory standardization and calibration of day mineral crystallinity and crystallite size data. *Journal of Metamorphic Geology*, 12(2), 141–152. <https://doi.org/10.1111/j.1525-1314.1994.tb00010.x>
- Xypolias, P. (2010). Vorticity analysis in shear zones: A review of methods and applications. *Journal of Structural Geology*, 32(12), 2072–2092. <https://doi.org/10.1016/j.jsg.2010.08.009>
- Zagorevski, A., Van Staal, C. R., McNicoll, V. J., Hartree, L., & Rogers, N. (2012). Tectonic evolution of the Dunnage Mélange tract and its significance to the closure of Iapetus. *Tectonophysics*, 568, 371–387.